Commissioning and Characterisation of the C-Band All-Sky Survey Southern Telescope

Dissertation by
Johannes Adotey Allotey

In Fulfilment of the Requirement
for the degree of
Master of Science

University of KwaZulu-Natal
Durban, South Africa

15 December 2015

Declaration

As the candidate's supervisor, I agree to the submission of this dissertation.

Dr. Hsin Cynthia Chiang

.....

I, ..., declare that

1. The research reported in this dissertation, except where otherwise indicated, is my original research.
2. This dissertation has not been submitted for any degree or examination at any other university.
3. This dissertation does not contain other persons' data, pictures, graphs or other information, unless specifically acknowledged as being sourced from other persons.
4. This dissertation does not contain other persons' writing, unless specifically acknowledged as being sourced from other researchers. Where other written sources have been quoted, then:
   (a) Their words have been re-written but the general information attributed to them has been referenced
   (b) Where their exact words have been used, then their writing has been placed in italics and inside quotation marks, and referenced.
5. This dissertation does not contain text, graphics or tables copied and pasted from the internet, unless specifically acknowledged, and the source being detailed in the dissertation and in the References sections.

Johannes Adotey Allotey

.....

15 December 2015

Acknowledgments

I will bless the LORD at all times: his praise shall continually be in my mouth. Glory to the LORD; for a wretch like me, has walked the face of earth and achieved a height such as this.

This work was fully funded by the Square Kilometre Array Africa. I am heavily indebted to them for making this work possible.

It has been invaluable and fun working on CBASS for the past two years, and I thank my supervisor, Dr. Hsin Cynthia Chiang, for allowing me to join a team of great minds and providing an environment full of training and learning. This work was possible with the efforts of the whole CBASS team and the hands of members of the Astrophysics and Cosmology Research Unit of this university especially Dr. Moumita Aich and Dr. Simon Muya Kasanda. I thank Professors Jonathan Leroy Sievers, Kavilan Moodley, Martin Bucher and Subharti Ray for impacting to me their knowledge in Computational Physics, Radiation Processes, Fluid Dynamics and Cosmology.

I owe much gratitude to Dr. Charles Judd Copley for allowing me study under his able arms and also using his PhD thesis as a guide for my work in the wilds. I am grateful to him and Heiko Heilgendorff for the long drives and walks to and from the wilds– a great experience indeed. To Ms. Lindile Danisa, Messrs Karan Naidoo and Musa Gasa for your administrative support in handling my financial burden.

I can't forget the labour of love exhibited by Messrs Byran Johnston, Søren Greenwood, Els Leonard and the whole ICS team in climbing mountains regarding Linux and remote machines for me. I also thank my friends, Byron Brassel, Kwazi Mthembu, Komi Assafinou, Ayanda Zungu, Monde Nasilele and Xavier Mbaale for useful discussions and also making the masters students office a lovely place to be.

I am extremely favoured to have met Dr. Jamie Leech, Luke Jew, Matthys Maree, Andre Walker, Siyabulela Tshongweni, Sizwe Seranyane, Michael Lesetja, and Isaac Moeng. I'm very grateful for your presence in the wilds and all your efforts in making this work possible. No words are enough to thank my family and all those who urged me on during my studies.

Abstract

The C-Band All-Sky Survey (CBASS) is a 5-GHz all-sky radio survey in both intensity and polarisation and with a resolution of 0.8°. These maps are obtained from telescopes in the northern and southern hemispheres and are useful for accurate subtraction of polarised Galactic synchrotron emission from high frequency cosmic microwave background experiments and also for probing the Galactic magnetic field structure. The southern system (CBASS-S) is a 7.6m Cassegrain telescope located at Klerenfontein, South Africa. To study the optics of CBASS-S, both the primary and secondary reflectors were examined. This dissertation describes the characterisation of the primary reflector using photogrammetry, a non-contact technique which makes use of photographs to acquire the exact position of the panels that comprise the mirror surface. Using this technique and MATLAB codes, dish deformations at different elevations and hence the surface accuracy were determined. The codes have been improved to automate adjustment values for panel alignment. The residual panel misalignments are used as inputs into the General Reflector Antenna Software Package in order to estimate the expected sidelobe levels.

The CBASS Collaboration

University of KwaZulu-Natal H. C. Chiang, J. L. Sievers, M. Aich, H. Heilgendorff, J. A. Allotey

California Institute of Technology S. J. C. Muchovej, T. J. Pearson, E. M. Leitch, C. Lawrence, A. Readhead, O. G. King, M. A. Stevenson, E. Quetin

University of Oxford M. E. Jones, A. C. Taylor, J. Leech, L. Jew, C. M. Holler (now at Hochschule Esslingen, Germany), P. Grimes, J. J. John

University of Manchester C. Dickinson, M. W. Peel, J. Zuntz, J. P. Leahy, R. Davis, S. Nakhuda, A. Barr, M. O. Irfan, K. Mata-Figueras, T. Armitage, R. Bhatawdekar, R. Davies of blessed memory

SKA Africa J. L. Jonas, C. J. Copley, R. Booth

Jet Propulsion Laboratory D. Jones

King Abdul Aziz City for Science and Technology Y. Hafez, F. Albaqami

Contents

List of Figures

List of Tables

Chapter 1

Introduction and Background

> Equipped with his five senses, man explores the universe around him and calls the adventure Science.
>
> Edwin Hubble

1.1 The Cosmic Microwave Background

1.1.1 The Big Argument

Early cosmologists always argued about the origin of the universe. There were two competing models; Steady State and Big Bang models which aimed to explain the origin of the universe, but there was no observational evidence to support their claims.

Steady State Model

The steady state model was first proposed in 1948 by Fred Hoyle, Hermann Bondi and Thomas Gold. In this model, the contents of the universe were the same at every point in time, which suggests the universe had no beginning and end. In 1929, with a 2.54 m reflecting telescope at the Mount Wilson Observatory, USA, Edwin Hubble measured the distances and motion of galaxies. He realised a few nearby galaxies were moving towards our Galaxy and majority of the galaxies were moving away. He discovered the universe was expanding. This discovery casted doubts over the steady state model since an expanding universe suggests an ever-decreasing density in increasing time. Supporters of the steady state model hypothesised the changes in density were a result of matter been continuously created out of nothing.

Big Bang Model

In 1949, the "Big Bang" was coined by Fred Hoyle during an interview on BBC radio. He vehemently rejected this model, a consequence of Hubble's discovery, claiming it was pseudoscience. In this model, the universe existed (in the beginning) in a very hot dense state and exploded, releasing baryons and photons which were tightly coupled. The universe was optically thick, which prevented the photons from

escaping, and hence the universe was opaque during this period. The universe began to expand and cool. As the universe expanded, the photons had insufficient energy to overcome the binding energy of hydrogen and hence the universe remained neutral. After this epoch (380,000 years into the expansion), the photons began to traverse freely throughout the universe. The transition referred to as recombination occurred rapidly that the photons emanated from a well defined region known as the surface of last scattering. These photons are called the cosmic microwave background (CMB), which was first predicted by Ralph Alpherin and George Gamow. These photons, if detected, would provide unrejectable evidence for the Big Bang.

1.1.2 The Big Discovery

In 1965, as Arno Penzias and Robert Wilson were using the Holmdel horn antenna at Bell Telephone Laboratories, USA, they detected an excess noise that they could not explain for. They repeated the experiment by looking at different locations on the sky, but the excess noise remained unchanged. Penzias and Wilson contacted Robert Dicke at Princeton university who, with his group, were building an antenna to measure the CMB. Dicke confirmed the excess noise was not originating from the horn antenna but the CMB. Penzias and Wilson received the 1978 Nobel Prize for Physics. This discovery proved the Big Bang was the preferred model for the origin of the universe.

A further look at the CMB

The discovery by Penzias and Wilson, caused several space missions to be launched to study the CMB in detail. Such missions included the Cosmic Background Explorer (COBE), Wilkinson Microwave Anisotropy Probe (WMAP) and Planck.

The Far Infrared Absolute Spectrophotometer on COBE showed that the CMB, which permeates our universe in all directions has a nearly perfect blackbody spectrum of temperature 2.7260 $\pm$ 0.0013 K [1]. The Planck radiation law in Equation (1.1) describes the specific intensity for blackbody radiation as functions of frequency, ν and temperature, T.

$$I(\nu, T) = \frac{2h\nu^3}{c^2} \frac{1}{e^{h\nu/kT} - 1} \tag{1.1}$$

h and k are Planck's and Boltzmann constants respectively and c, the speed of light. In the early universe, matter and radiation were in thermal equilibrium and the radiation has a blackbody spectrum as shown in Figure (1.1).

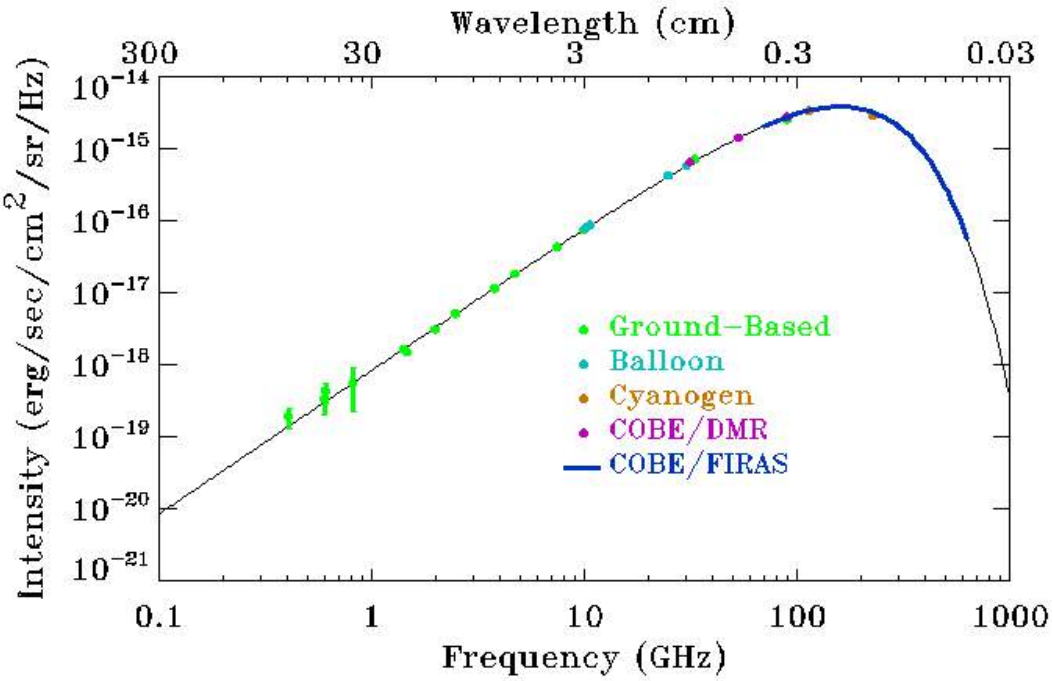

Figure 1.1: Intensity of the CMB versus frequency or wavelength as seen by COBE, balloon and ground based telescopes. Image: NASA science team.

The peak of the CMB curve falls in the microwave region which corresponds to a temperature of 2.725 K according to Wien's displacement law:

$$\lambda_{max} T = 0.290 \quad \text{cm deg} \tag{1.2}$$

T is temperature. The Wien's law describes the shift in blackbody spectrum as temperature increases. The shift in the peak of the blackbody spectrum is a measure of the spectral brightness of the blackbody as a function of wavelength.

COBE discovered the temperature of the CMB isn't totally uniform in all directions. These anisotropies; cold (blue) and hot (red) spots are regions of small density variations in the early universe as shown in Figure (1.2). These tiny density fluctuations are the seeds of stars and galaxies we see today. COBE's discovery was confirmed by the WMAP and Planck missions. The CMB temperature maps from the three missions are shown in Figure (1.2). The maps have temperature ranges of ± 200 μK with increasing image resolution from COBE to Planck.

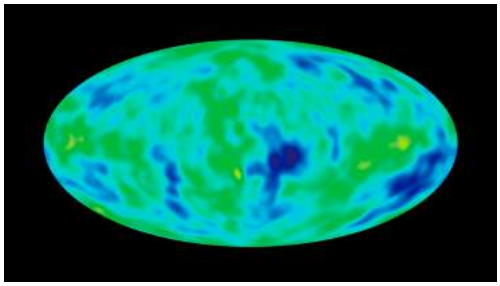

(a) COBE CMB temperature map.

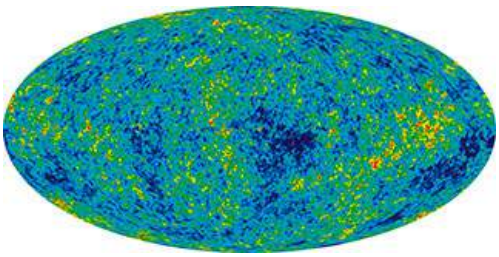

(b) WMAP CMB temperature map.

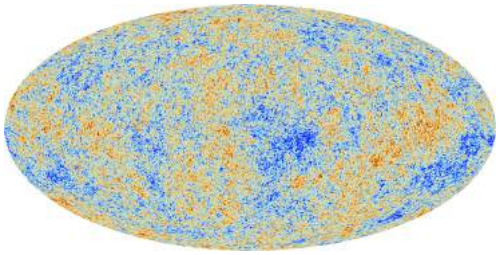

(c) Planck CMB temperature map.

Figure 1.2: CMB temperature maps from three missions. Images: NASA/Planck science teams.

1.1.3 Polarisation Anisotropy

As hot or cold incoming radiation shown in Figure (1.3) interacts with a free electron by Thomson scattering, the scattered radiation would be perpendicularly polarised to the direction of the incident radiation. If the incoming radiation were isotropic (dipole variation), the scattered radiation would be equally polarised in all directions, with no net polarisation. However, if the incoming radiation were anisotropic (quadrupole variation), the net scattered radiation would be linearly polarised because the poles of the variation are 90° separated.

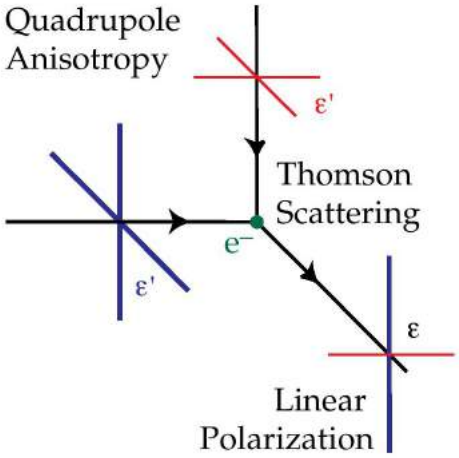

Figure 1.3: Polarisation by Thomson scattering of radiation. Blue colours (thick lines) represent hot and red colours (thin lines) cold radiation. Image: Figure 1 [2]

Linearly polarised radiation is described by the Stokes Q and U parameters, which are observer dependent. Q measures the difference in intensities in the x and y axes, while U measures the difference in intensities in a 45° coordinate system as described in Equation (1.3).

$$\begin{aligned} I &= I_{0^\circ} + I_{90^\circ} \\ Q &= I_{0^\circ} - I_{90^\circ} \\ U &= I_{45^\circ} - I_{135^\circ} \end{aligned} \tag{1.3}$$

I is total intensity; the sum of the intensity in both x and y axes. A more convenient way of determining the polarisation states is the use an observer independent approach shown in Figure (1.4).

E and B -modes

The CMB photons were scattered off free electrons during decoupling and the quadrupole anisotropies were imprinted onto the polarisation pattern of the CMB. The polarisation patterns are the E and B -modes. These modes were generated from scalar (density fluctuations) and tensor (gravity waves) perturbations in the early universe (plasma). The E-modes were produced due to scalar and tensor perturbations in the plasma and exhibits no handedness as shown in the upper panel of Figure (1.4). B-modes were generated from the quadrupole anisotropies created by perturbations due to gravitational waves in the early universe (inflationary B-mode) or gravitational lensing of E-mode at later times after the Big Bang. These phenomena created a curl pattern on the sky as shown in the bottom panel of Figure (1.4).

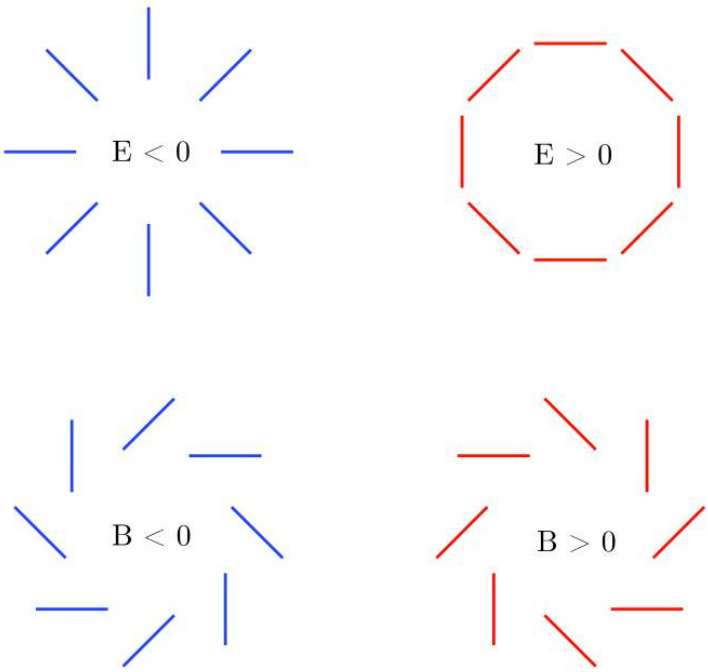

Figure 1.4: Polarisation decomposed into *E*- and *B*-modes. *E*-mode polarisation shows symmetry about the direction of travel while *B*-mode polarisation has a curl pattern. Image: Figure 3 [3].

The *B*-mode pattern generated as a result of gravitational lensing was first measured by the South Pole Telescope at 95 GHz and 150 GHz [4]. The faint inflationary *B*-mode signal is yet to be measured, and its detection would provide very strong evidence for cosmic inflation in the early universe. The detection of this signal is extremely difficult due to foreground contamination from our Galaxy and the weak gravitational lensing signal that mixes the *E*-mode with the *B*-mode signals; the former is the greatest difficulty for cosmologists. High sensitivity and control of systematics are needed to detect this faint signal.

The modes when used for CMB analysis are generated from the decomposition of Q+iU and Q-iU in terms of spin-2 spherical harmonics as shown in Equation (1.4) because they do not depend on orientation of the coordinate system on the sky ([5], [6]).

$$\begin{aligned}(Q+iU)(\hat{n}) &= \sum_{lm} a_{2,lm2} Y_{lm}(\hat{n}) \\ (Q-iU)(\hat{n}) &= \sum_{lm} a_{-2,lm-2} Y_{lm}(\hat{n})\end{aligned} \tag{1.4}$$

The ratio of the amplitudes of the gravitational waves to that of the density fluctuations in the early universe is referred to as tensor-to-scalar ratio, r which is a measure of the contribution of the B and E -modes to the CMB quadrupole. The most recent Planck measurement sets an upper bound limit at $r < 0.11$ at 95% confidence level [7].

BICEP2 and the *B*-mode Signal

In March 2014, Background Imaging of Cosmic Extragalactic Polarisation (BICEP)2 announced a 5σ detection of the primordial B-mode signal at 150 GHz with an amplitude corresponding to a tensor-to-scalar ratio value of $r = 0.20^{+0.7}_{-0.5}$ [8]. A joint analysis of BICEP2 and Planck (full sky polarisation survey from 30 to 353 GHz) data showed the initial claim of BICEP2 was highly dust correlated and reduced the significance to a non-detection for the primordial B-mode signal. The analysis further proved the detected signal was lensing B-modes at 7σ of an upper limit of $r_{0.05} < 0.12$ at 95% confidence [9]. Many other experiments such as SPIDER, Keck Array, POLARBEAR, EBEX and CLASS are continuing to search for the inflationary B-mode signal.

1.2 Foregrounds

As telescopes probe the sky for the CMB, emission at all frequencies from the sky, particularly from the Milky Way, contaminate this signal. This Galactic emission referred to as foregrounds, must first be removed from CMB data ([10]) to carry out precise cosmology. The dominant contaminants depend on the operating frequency of the observing telescope.

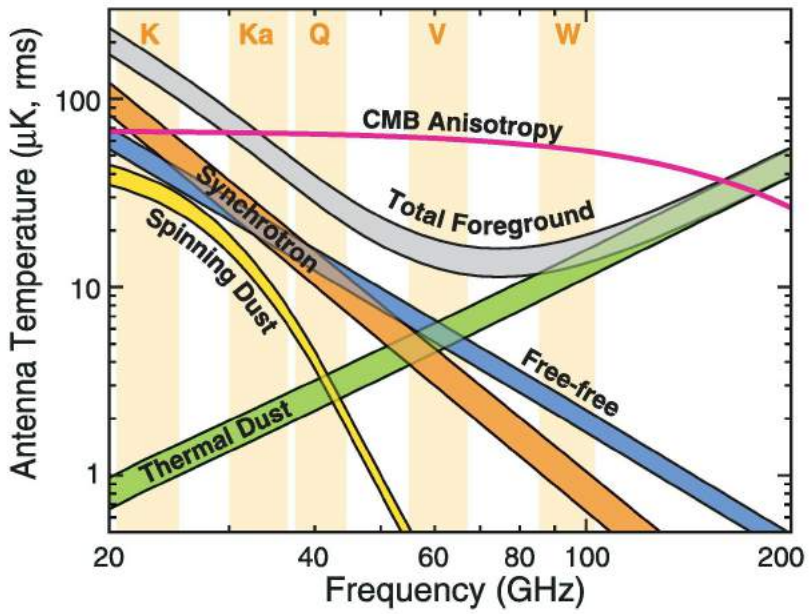

(a) The CMB and the various foreground emission processes at different frequencies.

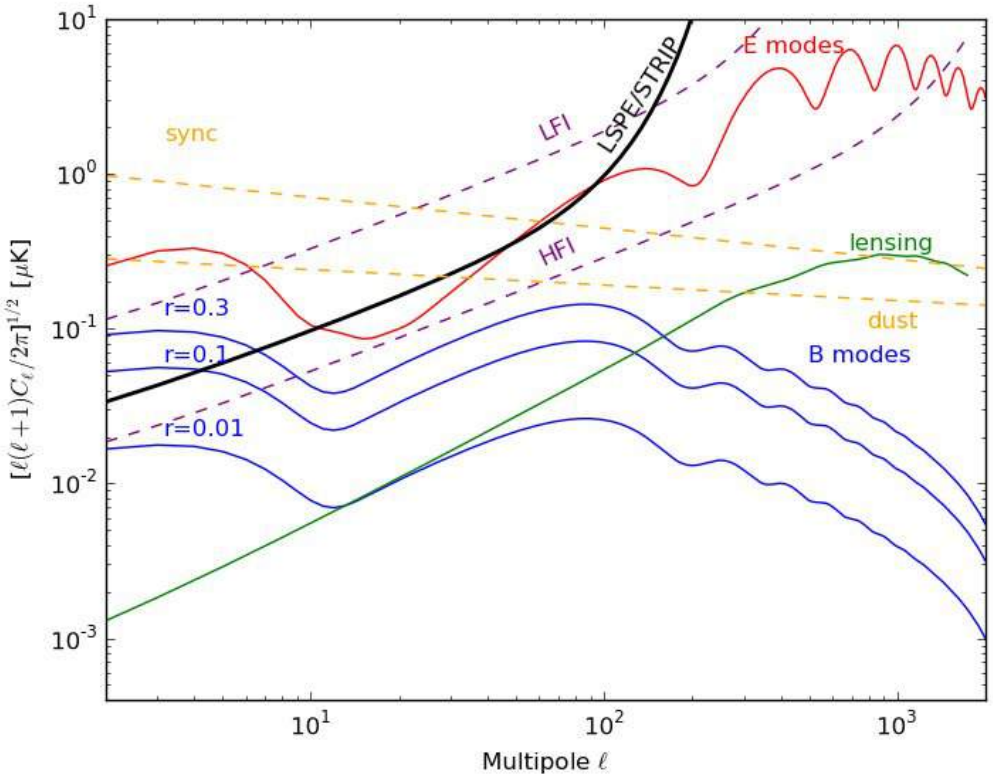

(b) The effect of the intensity of foreground emission on the detection of the cosmological B and E -modes signal at different tensor-to-scalar ratios. The detection of the B-modes is the most challenging as they are several orders of magnitude smaller than the foregrounds.

Figure 1.5: The CMB and the various foreground emission processes at different frequencies. Image: Figure 22 [11].

The four main physical processes responsible for these foregrounds as shown in Figure (1.5) are diffuse Galactic synchrotron emission, free-free emission, thermal dust emission, and anomalous microwave emission (AME).

Diffuse Galactic Synchrotron Emission

Diffuse Galactic synchrotron emission is the light seen when relativistic electrons spiral around a weak magnetic field as a result of Lorentz force. These accelerated electrons emit photons whose energies depend on the magnetic field and the energies of the electron themselves. The spectrum of the emitted radiation decreases with frequency [12]. Synchrotron emission comprises most of the observed Galactic emission at low frequencies, as shown in Figure (1.5)a. This emission is several orders of magnitude greater in intensity than the cosmological B-mode as shown in Figure (1.5)b and the emission must be accurately subtracted from CMB data to measure the cosmological signals.

Synchrotron radiation is linearly polarised and the polarisation is 10% - 75% of the total intensity [13]. Synchrotron measurements are an observational probe of Galactic magnetic field structure.

Free-free Emission or Thermal Bremsstrahlung

Free-free radiation is emitted due to Coulomb collisions between electrons and ions. In a hot plasma, the electrons are accelerated due to the collisions with the ions and thus radiate photons that exit the plasma if it is optically thin. For an interaction to occur, the electron must be in the vicinity of the ion; this minimum vicinity requirement is referred to as Thomson's cross section, σ_e with value 0.665 x 10^{-28} m^2. The frequency of the emitted radiation depends on the duration of the collision, and the spectrum of the radiation provides the temperature and emission measure of the plasma [12]. Free-free radiation is unpolarised.

Thermal Dust Emission

Thermal dust emission is a thermal process resulting from heating of the interstellar dust in the Galaxy to temperatures between 10 K and 100 K. The emission is a blackbody spectrum that depends on the size of the dust grains. Emission from the largest dust grains that are in thermal equilibrium with the local radiation field dominates the thermal dust emission [14]. This emission dominates at frequencies above 100 GHz, as shown in Figure (1.5)a. Thermal dust emission is 6% to 15% polarised [15]. This emission is much brighter than the cosmological B-mode as shown in Figure (1.5)b. This emission, like synchrotron emission must be subtracted from CMB data. Thermal dust emission is the greatest concern for all millimetric wavelength surveys such as BICEP2.

Anomalous Microwave Emission

Anomalous microwave emission (AME) was first detected at OVRO using two High Electron Mobility Transistor amplified radiometers to detect the anisotropies in the CMB at $7'$-$22'$ scales at 31.7 GHz and 14.5 GHz. Observations of 36 blank fields near the North Celestial Pole showed excess emission in certain fields at 14.5 GHz,

and this emission could not be explained by dust and synchrotron emission models. A strong correlation between the distribution of the excess emission, and the Infrared Astronomical Satellite 100μm maps of far-infrared dust emission were observed, indicating the 'strange' emission was dust-related [16]. The AME spectrum is most significant between 10 GHz - 100 GHz as shown in Figure (1.5)a, and spinning dust is a proposed mechanism to explain this emission. It is proposed the emission could arise from the electric dipole due to intrinsic dipole moment of the molecules and uneven charge distribution of the rapidly rotating tiny dust particles [17]. This emission is almost unpolarised. CBASS will search for new AME regions within our Galaxy.

1.2.1 CBASS and the *B*-mode Signal

CBASS's 5 GHz survey is high enough to be unaffected by Faraday rotation but low enough for mapping the synchrotron emission from our Galaxy. Foregrounds are very relevant for CMB experiments and CBASS will produce full sky synchrotron maps. CBASS is unable to detect CMB photons due to the lower frequency of operation as the CMB peaks at $\sim$300 GHz but the full sky synchrotron radiation maps will be useful for accurate subtraction of the Galactic synchrotron emission from *B*-mode polarimetry surveys.

1.3 CBASS Science Goals

CBASS will measure synchrotron emission from our Galaxy at 5 GHz and produce all-sky Stokes I, Q and U maps. The low frequency CBASS measurements will help in better understanding of the flattening of synchrotron spectrum at higher frequencies than the already available information from the 1.42 GHz ([18]) and 22.8 GHz ([11]) all-sky surveys [19]. These maps will allow for more accurate subtraction of the polarised Galactic synchrotron emission from *B*-mode experiments such as BICEP2, Keck Array, POLARBEAR, SPIDER, EBEX and CLASS.

The synchrotron emission data from CBASS will be used to map the local ($\leq$ kpc) Galactic magnetic field. CBASS will also be used to further study the distribution of anomalous dust and search for new regions of AME in our Galaxy.

Chapter 2

Primary Reflector Measurement Techniques

> A good forecaster is not smarter than everyone else, he merely has his ignorance better organised.
>
> Anonymous

The C-Band All-Sky Survey (CBASS), is a 5-GHz all-sky radio survey in both intensity and polarisation and with a resolution of 0.8°. The CBASS maps are obtained from telescopes in the northern and southern hemispheres. The northern system (CBASS-N) consists of a 6.1 m Gregorian telescope located at the Owens Valley Radio Observatory (OVRO), California, USA, and the southern system (CBASS-S) is a 7.6 m Cassegrain telescope located at the MeerKAT support base, Klerenfontein, Northern Cape Province, South Africa. The telescopes received by the CBASS team were without detailed diagrams and documentation which leaves the optics of the instrument unknown. To use the telescope as an imaging tool, the primary reflector was measured in order to effectively design the secondary. This chapter describes the technique used for measuring the primary reflector, modelled best fit shape and how panels were aligned to achieve the modelled shape.

2.1 The CBASS Instruments

The telescopes donated to the project were originally designed for telecommunication purposes. To serve as imaging instruments, the circularly symmetric primary reflectors were measured using photogrammetry and the secondaries, redesigned using Galindo's theory of shaped dual reflectors [20]. The shapes and sizes of the primary reflectors differed, and a common beam pattern is required for full sky maps hence different optical configurations were used. The different optical configurations allowed the same low sidelobe horn to be used for both telescopes. CBASS-N and CBASS-S have analog and digital backends respectively. CBASS-S's backend makes processing of received signals easy and allows radio frequency interference to be removed easily. The CBASS target noise is 0.1 mK/deg^2 in Stokes Q and U.

2.1.1 The Northern Telescope

The 6.1 m telescope was designed as a prototype for the National Aeronautics and Space Administration Deep Space Network, which is the largest and most sensitive telecommunication system in the world. The telescope was donated by the Jet Propulsion Laboratory and developed by the CBASS team for imaging.

Figure 2.1: The northern system.

A Gregorian (concave ellipsoidal) optical configuration was used for the northern system. Metallic absorbing baffles were mounted around the primary reflector as shown in Figure (2.1), which minimises spill-over of incoming radiation to ground. Also around the secondary, are absorbing baffles that reduce cross-polar response. These absorbing baffles minimised the sidelobes at 50° and 110° [20]. The secondary reflector is located on a foam cone support to minimise scattering of incoming radiation compared to quadrupode support legs.

2.1.2 The Southern Telescope

Circularly symmetric 7.6 m low-earth-orbit communication telescopes were donated by Telkom SA SOC Limited to the CBASS team. The first telescope was moved from the Telkom site to the Hartebeesthoek Radio Astronomy Observatory (HartRAO), Gauteng, South Africa for receiver commissioning as shown in Figure (2.2)a. The second telescope was moved to the MeerKAT support base in Klerefontein, Northern Cape Province, and the receiver was recommissioned in May 2014, which served as observing telescope for CBASS-S as shown in Figure (2.2)b.

A Cassegrain (convex hyperboloid) optical configuration was used for the southern system. The secondary reflector was designed to allow only 6.1 m diameter of the primary to be illuminated to attain the same illumination area as the northern system hence any spillover of incoming radiation is reflected to the sky.

The southern system is a continuous comparison radiometer receiver that removes the effect of gain variations in the amplifiers from the system. In the continuous comparison radiometer, the sky signal is referenced to a stabilised load in the signal chain using a 180° hybrid. CBASS-S measures the power of astronomical sources by separating the sky voltage from the reference load voltage.

(a) The telescope used for receiver testing at HartRAO, Guateng, South Africa.

(b) The operational southern system at the MeerKAT support base, Klerenfontein, South Africa.

Figure 2.2: The CBASS telescopes

2.1.3 Differences between CBASS-N and CBASS-S

The differences between the CBASS telescopes are shown in Table (2.1).[1]

	CBASS-N	CBASS-S
Location	OVRO, California Latitude 37.2°	MeerKAT Support Base Klerenfontein, Latitude −30.7°
Sky Coverage	Northern sky	Southern sky
Bandwidth	4.5 - 5.5 GHz across 1 channel	4.5 - 5.5 GHz across 128 channels
Backend	Analogue	Digital
Optical Configuration	Gregorian	Cassegrain
Dish Diameter	6.1 m with absorbing baffles	7.6 m under illuminated
T_{sys}	∼20 K	∼22 K
Start of observation	November 2012	—
End of observation	May 2015	—

Table 2.1: CBASS-N versus CBASS-S.

2.2 Close Range Photogrammetry

Close range photogrammetry is a non-contact technique that makes use of photographs to acquire the exact position of the panels that form the primary telescope. The technique was used via the image processing software package called PhotoModeler[2] that created a three-dimensional (3D) point image of the entire surface. The accuracy to primary reflector diameter ratio for photogrammetry is typically 1:30,000+[3].

[1] Private communication with Heiko Heilgendorff.

[2] PhotoModeler tool described in http://www.photomodeler.com/products/modeler/default.html

[3] From PhotoModeler official website: http://www.photomodeler.com/kb/entry/63/

2.3 Camera Calibration

Camera calibration was the first activity undertaken before any photogrammetry measurements were taken. PhotoModeler requires information about the camera to be used for this project, hence a need to accurately calibrate the camera. To perform this task, readily available calibration sheets were printed and photographs of the sheets were taken. Calibration sheets have geometrical and circular targets printed on them to allow image processing software to recognise them in photographs. The photographs of the calibration sheets taken are used to run a calibration project in PhotoModeler so the software can obtain camera properties such as focal length, aperture, shutter speed, white balance, image resolution and International Organisation of Standardisation (ISO). Camera calibration is performed each time the camera body or lens is changed. 28-mm focal length camera was used for our measurements. The three camera calibration types are Single Sheet Calibration (SSC), Multi Sheet Calibration (MSC), and Field Calibration (FC). SSC and MSC make use of photographs of the calibration sheets while FC makes use of photographs of the actual specimen. In SSC, one calibration sheet is used, and the technique is appropriate for specimens less than 1.5 m in all dimensions. MSC is used for specimens greater than 1.5 m in all dimensions, and multiple sheets are used. We used MSC because the primary surface of CBASS-S is 7.6 m in diameter.

Multi Sheet Calibration

Calibration sheets were printed and arranged in a square 2x2 matrix and, with the help of a tripod, photographs were taken from four different locations around the sheets for profile and landscape orientations of the camera, shown in Figure (2.3). The photographs of the calibration sheets obtained were exported into PhotoModeler, and an automated camera calibration is run for the camera parameters. For the 28 mm lens, we obtained an image coverage of 70% and an overall RMS residual of 0.1 pixel (which is less than the 1 pixel requirement).

(a) Calibration sheet in profile orientation of camera.

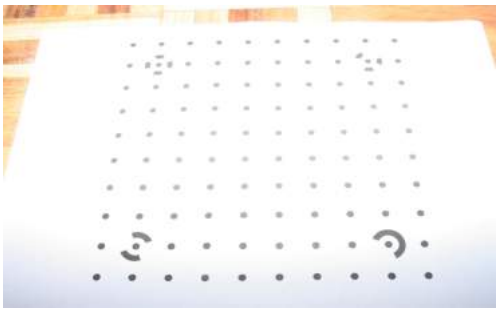

(b) Calibration sheet in landscape orientation of camera.

Figure 2.3: MSC calibration.

2.4 Photogrammetry Targets

Geometrically coded and circular uncoded black adhesive stickers in Figure (2.4)a, were hand pasted on the primary reflector. The geometrically coded targets are used for panel identification and scaling purposes. The uncoded circular targets are for achieving sub-pixel resolution in point positions in PhotoModeler. These targets are necessary for PhotoModeler to map out the shape of the primary reflector.

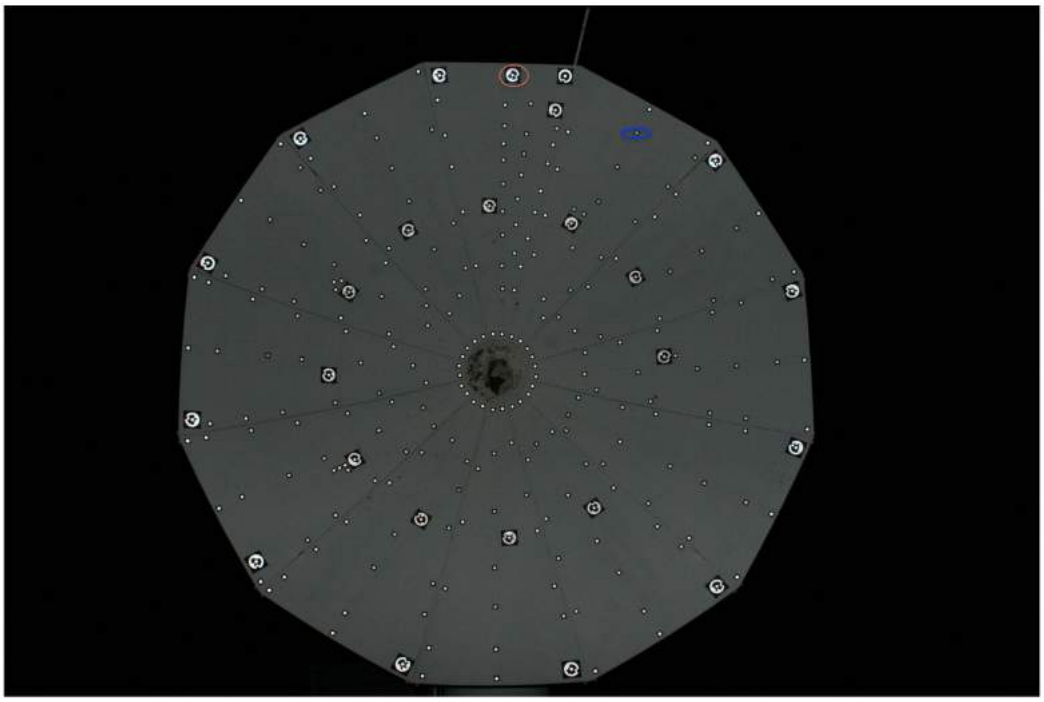

(a) A photograph of the primary reflector at night showing the geometrically coded (shown with red circle) and uncoded circular optical targets shown with blue circle.

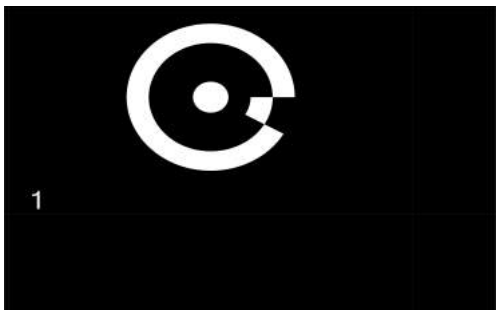

(b) Sample geometrically coded target used on the primary reflector.

Figure 2.4: Targets required for processing in PhotoModeler.

The positions of all the geometrically coded targets on the primary reflector are shown by the black and red asterisks in Figure (2.5). The red asterisks in the figure are used for panel identification with label; *Panel Number* to the left of the hyphen and *Target ID* to the right of the hyphen.

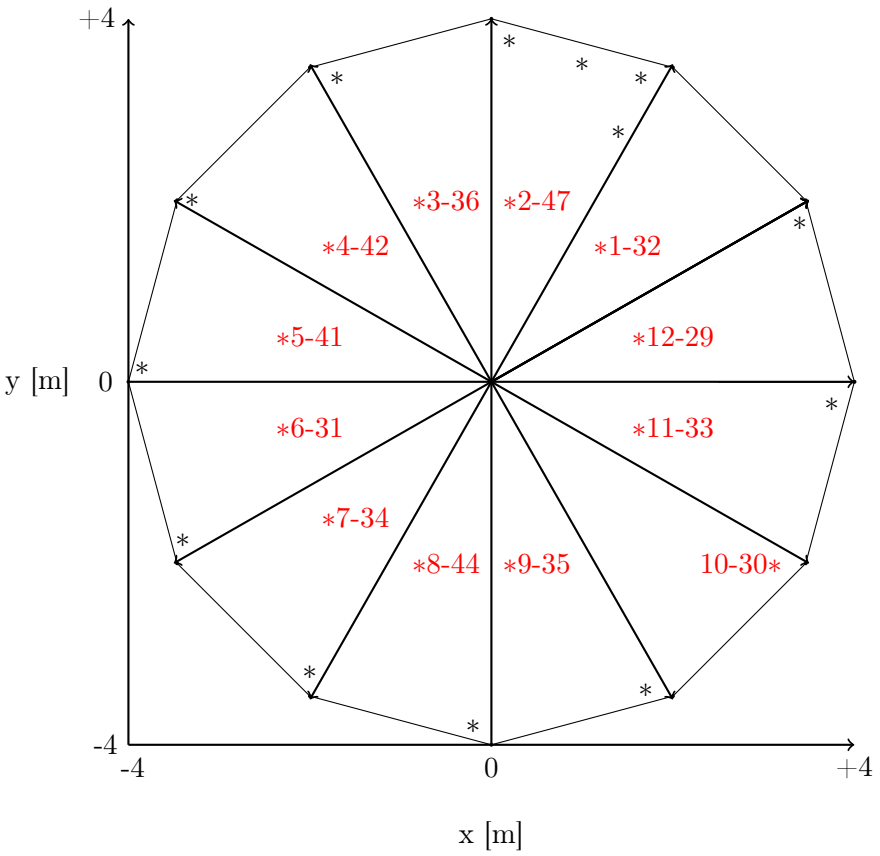

Figure 2.5: Geometrically coded targets on the primary reflector. The circular uncoded targets are not displayed here.

Scaling of Photogrammetry Project

It is of utmost importance that we scale our project in PhotoModeler to match the dimension of the primary reflector. PhotoModeler provides two options for scaling: the two-point and three-point methods. The two-point method measures the distance between two selected points on a panel, while the three-point method measures the positions (in degrees) of three selected points on a panel. Two coded targets on Panel 9 were chosen and a tape measure was used to measure the distance between them. The distance of separation is shown in Figure (2.6). The distance of separation was always used as a reference and checking for this distance in PhotoModeler is helpful for accurate scaling. We always used the three-point method for our scaling and cross checked with the two-point approach for all photogrammetry measurements. The targets used for the three point scaling are marked as blue asterisks on Panel 2 in Figure (2.6) and, their positions are displayed in Table (2.2). Incorrect scaling leads to incorrect dimensions of the primary reflector and panel identification problems.

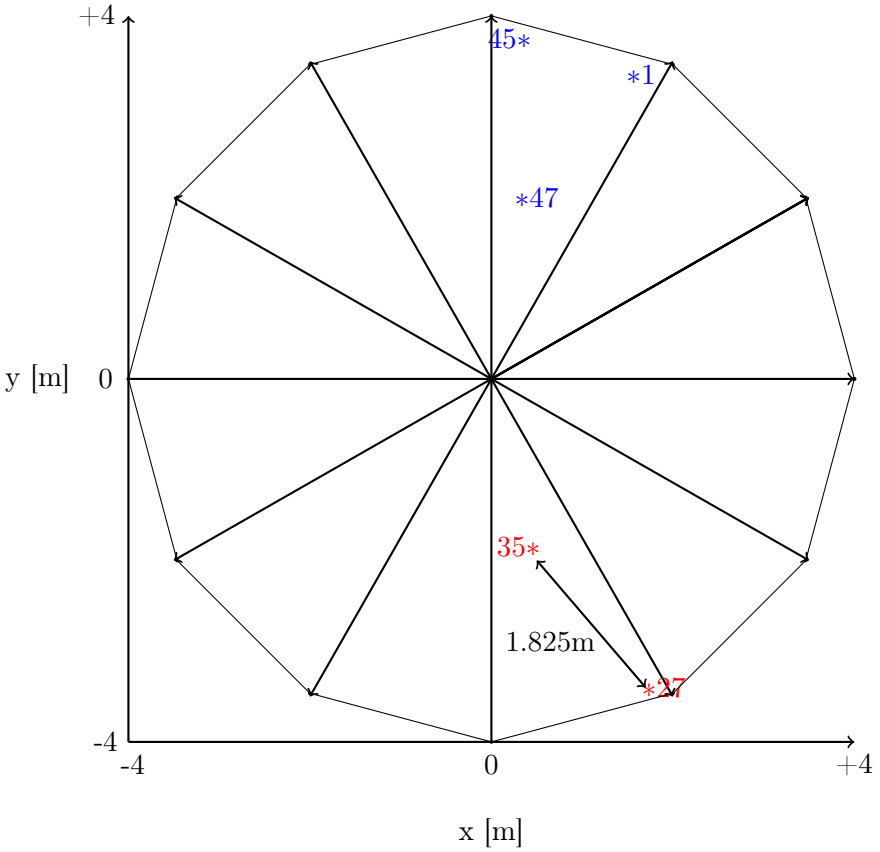

Figure 2.6: Targets used for scaling in photogrammetry project.

Target ID	x position	y position	z position
1	-1.817°	-5.982°	-12.537°
45	-0.266°	-5.489°	-12.52°
47	-1.323°	-4.278°	-13.386°

Table 2.2: Three-point scaling measurements as determined by PhotoModeler. Errors in the positions of these points are discussed in Subsection (2.5).

2.5 Photographing of the Primary Reflector

After camera calibration, photographs of the primary reflector were taken. The primary reflector was positioned at elevation (el) = 85° for most of our measurements and remained fixed throughout a single exercise. Photographs of the primary reflector were taken from various angles and heights with the help of a crane, ensuring most of the primary reflector was captured in the camera's field of view. The crane is usually positioned 5 m away from the primary reflector for good contrast of the targets in order for PhotoModeler to recognise them in the photographs. We usually take over fifty photographs due to requirements on target contrast and separation angles of photographs.

Reduced Photogrammetry

The processing of the photographs of the primary reflector in PhotoModeler is referred to as reduced photogrammetry. Photographs with good target contrasts and separation angles are used in reduced photogrammetry. The geometrically coded targets on the primary reflector are easily recognised by PhotoModeler via least square fitting approach and the circular uncoded target positions are determined by centroid fitting. These approaches allow PhotoModeler to create a 3D point image of the primary reflector.

Photogrammetry Data Structure

The data from PhotoModeler is a seven column dataset showing ID numbers of targets, the 3D positions of the points and their respective errors. We represent this data as target *Target ID*, *x*, *y*, *z*, *xerr*, *yerr* and *zerr* respectively.

2.6 Surface Function Measurement

The primary surface was modelled by Christian Holler at the University of Oxford, England by using the first photogrammetry data. The shape of the primary reflector was modelled using the surface function in Equation (2.1) that describes the depth of the reflector, z, as a function of radius, r. Equation (2.1) provides the shape of the primary reflector we aimed to achieve after assembling all twelve panels.

$$z(r) = -0.000524r^5 + 0.004680r^4 - 0.016472r^3 + 0.120840r^2 - 0.015305r \quad (2.1)$$

2.7 Specification for CBASS

The Ruze formula relates the forward gain of the primary reflector to Gaussian distributed uncorrelated random errors on the primary reflector. The formula is a measure of the power loss due to irregularities on the surface of the primary reflector [21]:

$$\eta_s = exp\left[-\left(\frac{4\pi\sigma}{\lambda}\right)^2\right] \quad (2.2)$$

η_s is the surface efficiency, σ is the RMS error and $\lambda = 60$ mm for CBASS since we are operating at a frequency of 5 GHz. From the Ruze formula in Equation (2.2), CBASS aims to achieve a forward gain loss of less than 10% and hence a forward gain better than 0.9 corresponding to RMS error better than 0.5 mm. From Equation (2.2), the forward gain falls rapidly as the rms error in wavelengths exceed $\frac{1}{16} \approx 0.06$ as shown in Figure (2.7). For CBASS, the expected forward gain or surface efficiency is shown in Figure (2.7) and obtained at rms error in wavelength of 0.01.

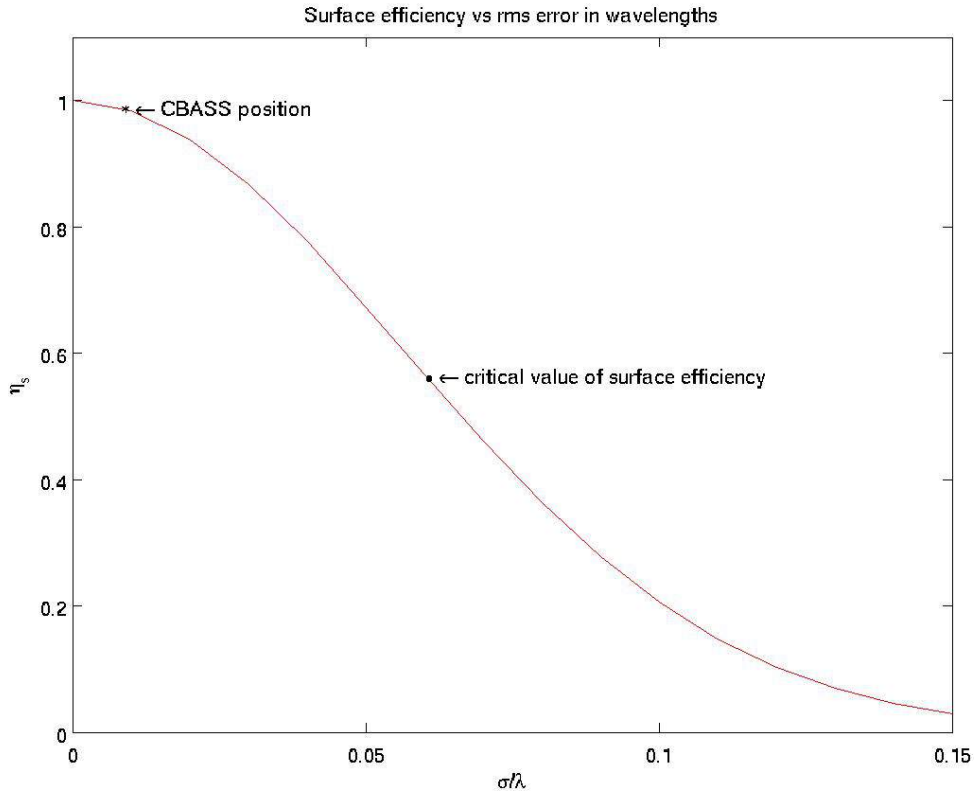

Figure 2.7: Ruze scattering curve.

Chapter 3

Achieving the Modelled CBASS Primary Surface

> This is precision science, so we cannot do things by 'eyeballing'. Allow the code to do what you need and you will overcome the mishaps you've had in the past.
>
> Hsin Cynthia Chiang

The panels that comprise the primary reflector were separately removed at the Telkom site and transported to Klerenfontein. The panels were then assembled to form the primary reflector of the observing telescope as shown in Figure (3.1). Photogrammetry was carried out to determine the panel misalignments (deviation from the modelled shape as described in Equation (2.1)). This chapter describes the techniques used in obtaining the modelled shape and the surface profile of the primary reflector.

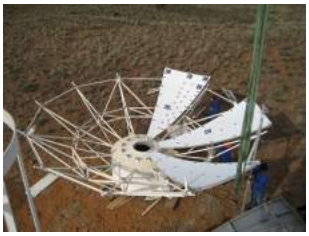

(a) Assembling all panels of the primary reflector.

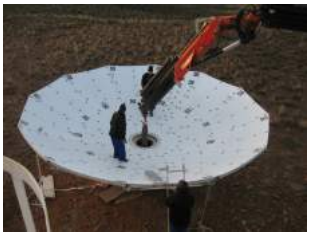

(b) Lifting the assembled primary reflector with a crane.

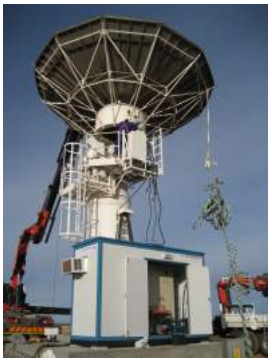

(c) Mounting the assembled primary reflector onto the base.

Figure 3.1: Assembling CBASS-S primary surface. Images: Charles Copley.

3.1 Analysis of the Primary Reflector Surface

The dataset obtained from PhotoModeler described in Subsection (2.5) was read into MATLAB and fitted to an axially symmetric paraboloid to align the axis of symmetry with the z-axis of the primary reflector. The deviations from model in Equation (2.1) were plotted. These deviations represent the panel misalignments and are used to determine the sidelobe levels. The MATLAB codes were developed by Charles Copley during his PhD at the University of Oxford, England.

In this section, I will present the results of the photogrammetry measurements taken up to the time of submission of this dissertation. The step by step procedure used in panel iteration shall also be described.

Structure of Panels of the Primary Reflector

Each panel has six bolts which, when adjusted, allows panels to be correctly positioned in order to achieve the shape described in Equation (2.1).

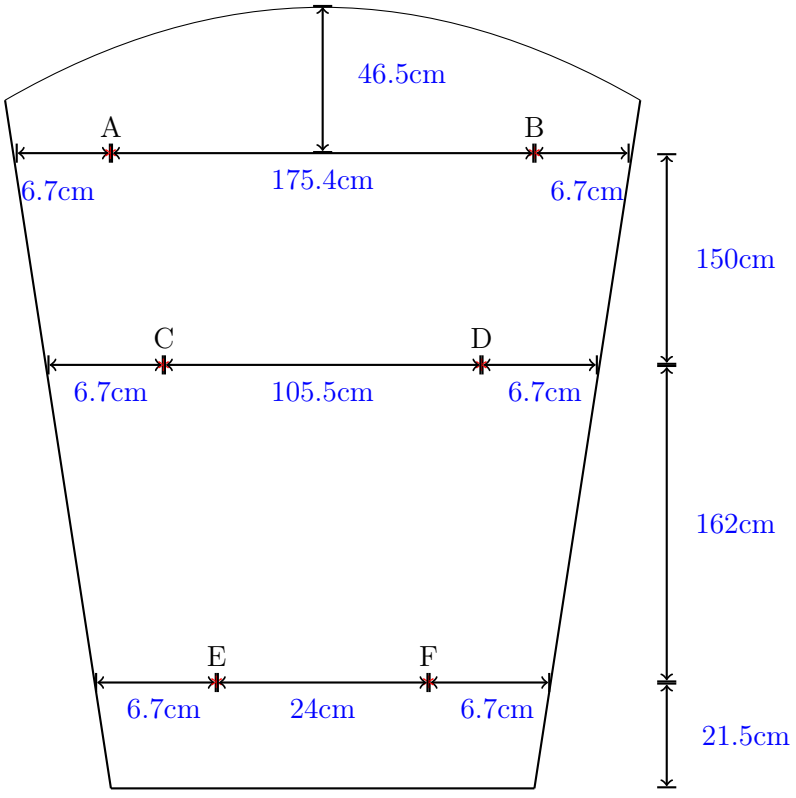

Figure 3.2: Structure of a panel of the primary reflector as seen from the ground with 'A' furthest to the left. The asterisks represent the bolt positions (or adjustment points) with their corresponding labels.

3.1.1 2014 Measurements

May 2014

After the panels had been assembled and the primary reflector mounted onto the base to form the CBASS-S system, the first set of photogrammetry measurement was taken in May and the result shown in Figure (3.3)a. The panel misalignments improved after each iteration with a reduction in the RMS errors as shown in Figures (3.3)b and 3.3c.

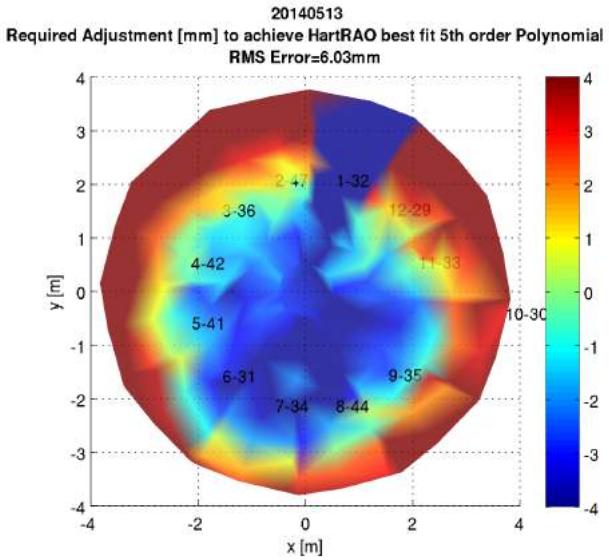

(a)

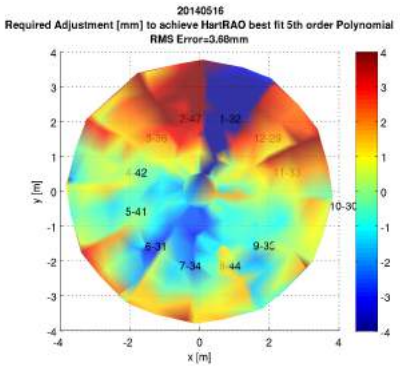

(b)

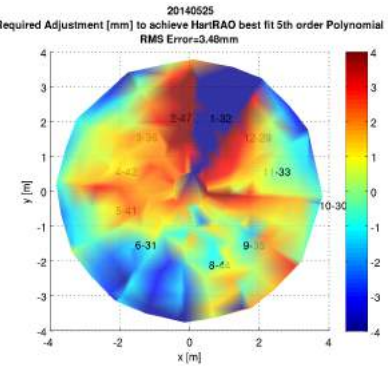

(c)

Figure 3.3: In all plots, the colour map represents deviations of panel positions from the model in Equation (2.1) over the entire 7.6 m diameter of the primary reflector. The colour bar is in units of millimetres (mm). In all plots, all the panels were iterated except Panel 1. In plots (a), (b), and (c), the average RMS calculated over the entire surface is 6.03 mm, 3.68 mm, 3.48 mm, respectively. All three measurements were taken with the primary reflector taken at elevation (el) = 5°.

Formalism for Panel Iteration

Panel 1 was intentionally lifted to serve as a reference panel and was adjusted to align with the other panels on May 26. As shown in Figure (3.3)a, the deep blue colour on Panel 1 depicts a lowering of the panel is required. The iteration mechanism is set as follows:

1. A complete turn of a bolt (adjustment point) is equivalent to a 1.75 mm shift in panel position.

2. Red colours (positive values) and blue colours (negative values) indicate that lifting and lowering of panels are required, respectively, to achieve the best shape of the primary reflector.

3.1.2 Dish Deformation at Different Elevations

21 June 2014

On 21 June 2014, a measurement at each elevation (el) = 5°, 45°, and 85° was carried out to investigate the effect of elevation on primary reflector deformations. Panel iterations were not done between measurements. The RMS errors varied for each el as shown in Figures (3.4)a, (3.4)c and (3.4)e.

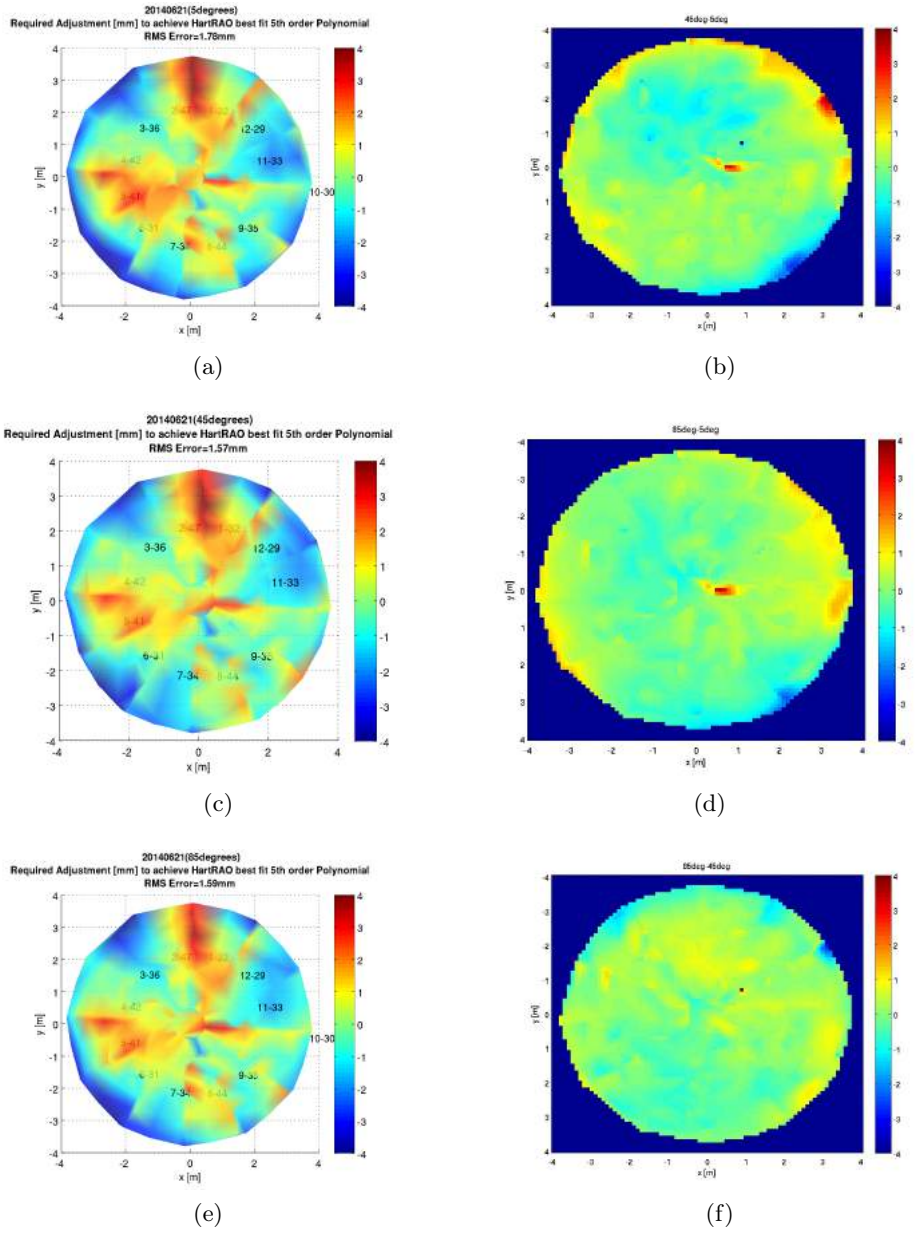

Figure 3.4: Plots (a), (c) and (e), are the surface of the primary reflector taken at elevation (el) = 5°, 45° and 85° respectively. The RMS errors in these plots are 1.78 mm, 1.57 mm and 1.59 mm respectively. The difference between the various elevation positions in plots (b), (d) and (e), is mostly $\sim < 1$ mm across the face of the primary reflector.

To determine the maximum of ∼0.2 mm change in the RMS errors, the differences between the el measurements were determined. The difference plot in Figures (3.4)b, (3.4)d and (3.4)f show small variations in the surface profiles at different el but not the source of the variation. To determine whether the elevation differences were dominated by errors in photogrammetry measurements or real changes in panel positions, we generated the colour profile of the primary reflector for 4 June 2015

measurement using different set of photographs and the result is discussed in Section (3.4). Panel iteration was done after these measurements using the 85° result because we opted to take all subsequent measurements at el = 85° if the best fit shape was not achieved after the iteration. Subsequent June measurements were carried out at el = 85° and panel iteration was done between them which improved panel alignments as indicated by the minimal fall in RMS error as shown in Figure (3.5).

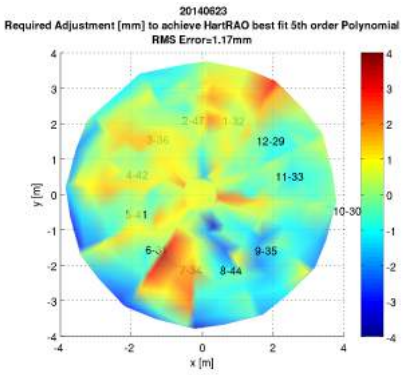

(a) Surface profile of the primary reflector after iterating panels with data from Figure (3.4)e. There was a 0.4 mm fall in RMS error indicating good panel iteration.

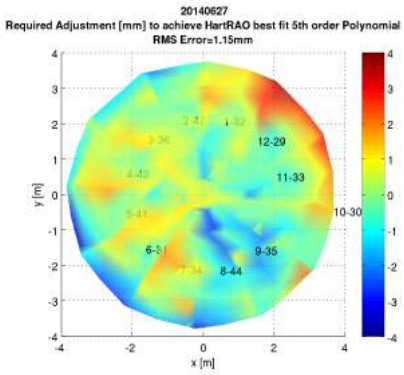

(b) After panel iteration with data from Figure (3.5)e, Panel 7 position improved but Panels 1, 11 and 12 position worsened at the edges leading to a 0.02 mm improvement in RMS.

Figure 3.5: Panel iteration between measurements improved the RMS by 0.02 mm.

We were still high in RMS error as described in Subsection (2.7) so we carried out further measurements and iteration.

September 2014

The telescope's weather station was hit by lightning, thereby damaging the weather station, control computer, USB/fibre converter, GPS unit, Reconfigurable Open Architecture Computing hardware (ROACH) analog to digital converters that control the one pulse-per-second signal from the GPS unit and the servo controller. These broken parts kept the telescope idle for three months and we returned to site to fix these parts and also carried out another measurement with the primary reflector at el = 85°. The result is shown in Figure (3.6).

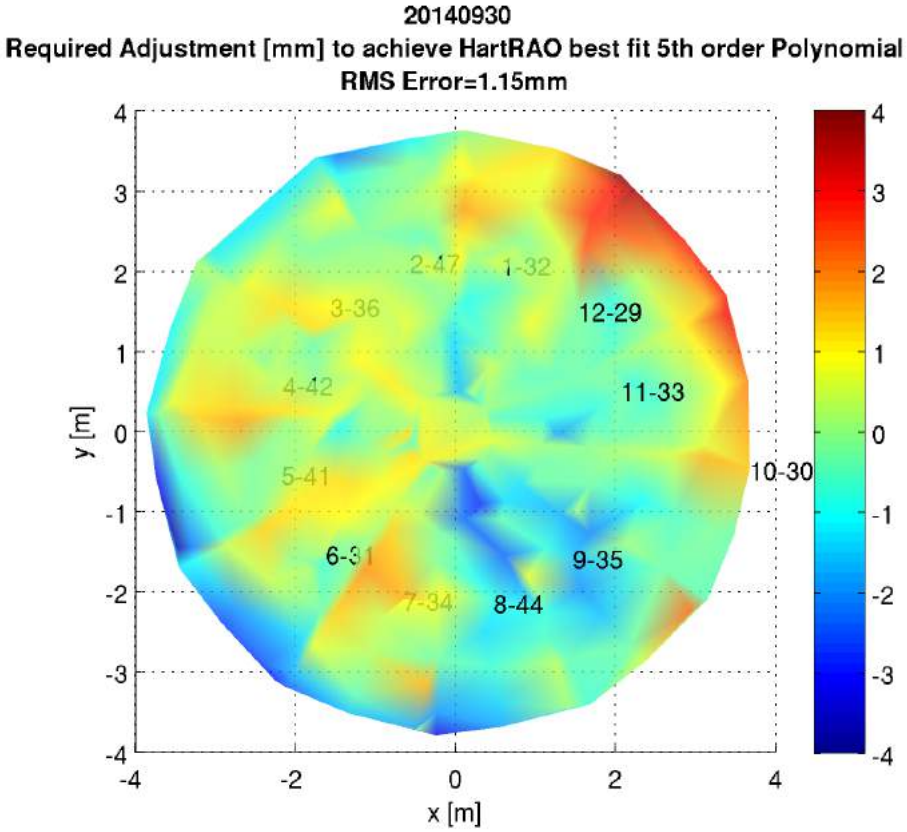

Figure 3.6: The panel positions did not change after the telescope had been idle for three months depicting the environmental conditions on site do not affect the panel positions.

No panel iteration was done before this measurement was taken. The panel positions and the RMS error did not change from Figure (3.5)b which demonstrate that the panel positions were unaffected by surrounding conditions (wind, rain and temperature).

October 2014

The panels were iterated before each measurement was taken but the RMS error increased for 4 -7 October as shown in Figures (3.7a, 3.7b and 3.7c), which was surprising.

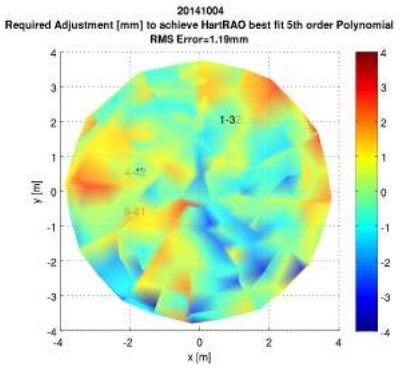

(a) 4 October measurement. Sudden increase in RMS error due to iteration at wrong adjustment points.

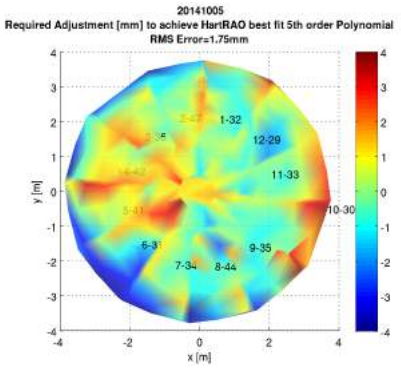

(b) 5 October measurement. Sudden increase in RMS error due to iteration at wrong adjustment points. Panel 1 was intentionally lifted again to verify our formalism for panel iteration.

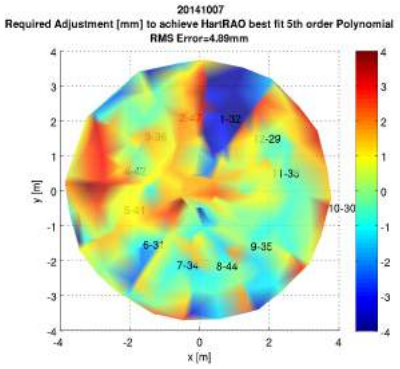

(c) 7 October measurement. The deep blue colour on Panel 1 indicates a lowering of the panel is required to align with the others and so verified our formalism for panel iteration (2).

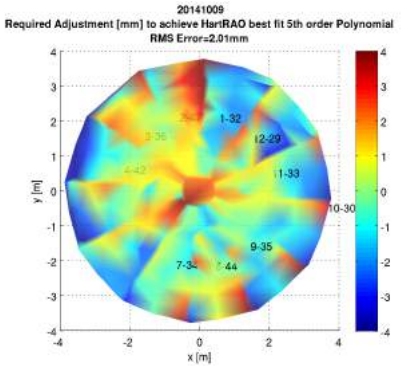

(d) 9 October measurement. Iteration was done at the right adjustment points which improved the RMS error.

Figure 3.7: October measurements made at el = 85°. The fluctuation in RMS errors was due to human errors.

We rechecked our formalism for panel iteration by lifting the reference panel by three complete turns of all six bolts shown in Figure (3.2). The effect of lifting the reference panel was seen as deep blue in Figure (3.7)c and contributed to a further increase in RMS error. The deep blue colour indicates our formalism for panel iteration (2) was right hence a need to probe further into the cause of the increase in RMS errors. Comparing the expected adjustment values and those made at the various bolts, we realised we had adjusted the wrong bolts. The iteration was then made at the correct adjustment points, reducing the RMS error to 2.01 mm as shown in Figure (3.7)d. Panels were then iterated without any photogrammetry measurement due to overlapping panel edges. The edges of the panels began to overlap after several upward iterations and there was a need to separate these edges before any fine adjustments can be done correctly. Only a few were successfully separated and the panel alignments were done by eye using Panel 1 as a guide. After

iterating panels by eye, there was a significant increase in RMS to 2.14 mm as shown in Figure (3.8)a. With strong winds and heavy rains, we only iterated some of the bolts on a few panels that were largely misaligned in Figure (3.8)a and the result is shown in Figure (3.8)b.

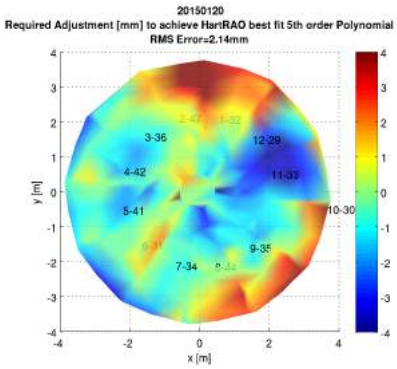

(a) The surface of the primary reflector after iteration was done by eye. The RMS error increased from 2.01 mm to 2.14 mm because of the errors accompanying iteration by eye.

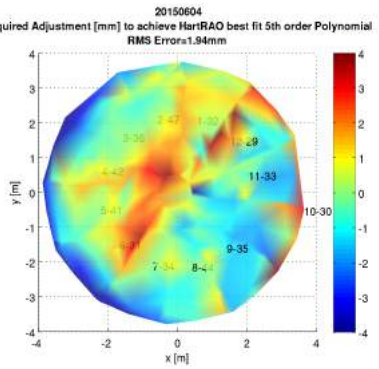

(b) Only a few bolts on Panels 1, 2, 11 and 12 of Figure (3.8)a were iterated but Panels 3 to 10 showed significant change in positions. This measurement was taken with the primary reflector at el = 85°.

Figure 3.8: Comparing surface profiles of the primary reflector before and after a few bolts of panels were iterated.

We did not expect panels that were not iterated to change position but Figure (3.8)b shows otherwise. The shift in panel position could be due to the overlapping panels that caused a shift in other panels during iteration. The adjustment values made on the few bolts (bolt positions shown in Figure (3.9)) of some of the panels are shown in Table (3.1).

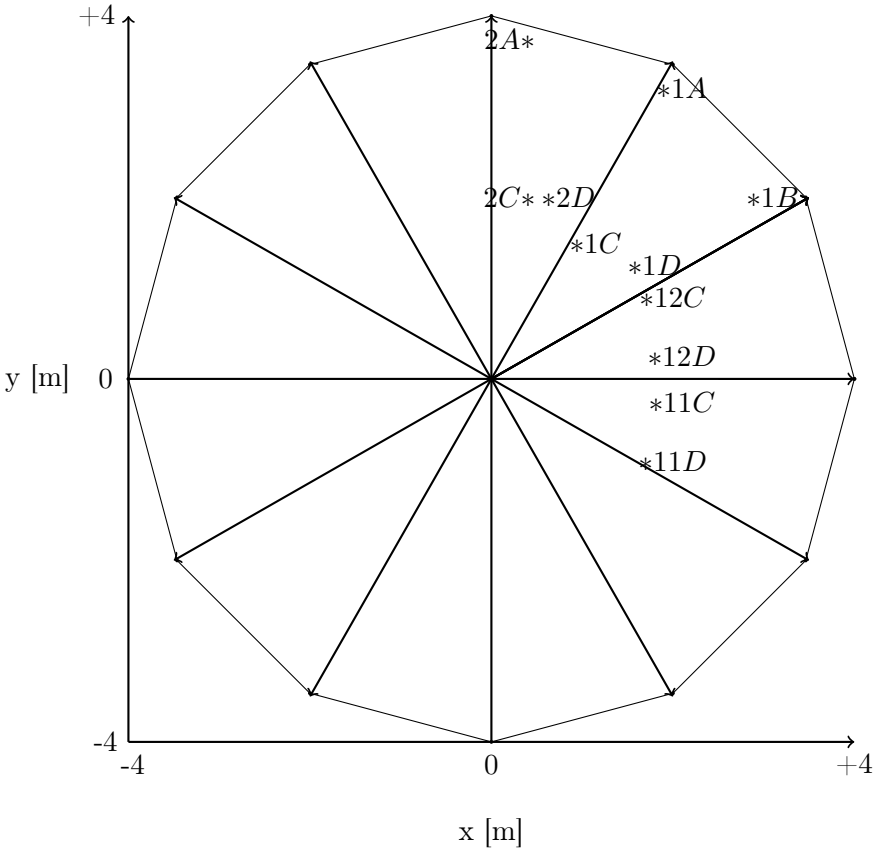

Figure 3.9: The adjusted bolts in Figure (3.8)b shown in black asterisks with 'A' furthest to the left as seen from the ground.

Panel Number	mm Adjustment	Number of Turns (mm value/1.75)
Panel 1	A = 2 B = 4 C = 1 D = 1.5	A = 1.1 B = 2.3 C = 0.6 D = 0.9
Panel 2	A = 4 C = 1 D = 1	A = 2.3 B = 0.6 C = 0.6
Panel 11	C = -2 D = -1	C = -1.1 D = -0.6
Panel 12	C = -3 D = -0.5	C = -1.7 D = -0.3

Table 3.1: The adjustment values made on the few bolts in Figure (3.9).

To probe further the cause of the shift in positions for panels not iterated, the surface profile for 4 June 2015, were regenerated using different sets of already available photographs. The regeneration of the surface profiles of the primary reflector is discussed in detail in Section (3.4.)

3.2 Separation of Overlapping Panels

To carry on with iterations to obtain the modelled shape of the primary reflector easily, we lowered the panels except for a few, by six turns (10.5 mm) of all bolts, separated all panels with overlaps and then realigned them. The iterations made on the bolts are shown in Table (3.2).

Panel Number	Turns	Panel Number	Turns
Panel 1	A = -6 B = -6 C = -7 D = -6 E = -6.5 F = -6	Panel 7	A = 0 B = 0 C = 0 D = 0 E = -2.5 F = 0
Panel 2	A = -6 B = -6 C = -0.5 D = -6 E = already loose F = already loose	Panel 8	A = -6 B = -6 C = -6 D = -6 E = -6 F = -6
Panel 3	A = -1 B = 0 C = 0 D = 0 E = -3 F = -2.5	Panel 9	A = -6 B = -6 C = -6 D = -6 E = -6 F = -6
Panel 4	A = 0 B = -0.5 C = 0 D = 0 E = -3 F = 0	Panel 10	A = -6 B = -6 C = -6 D = -6 E = -6 F = -6
Panel 5	A = 0 B = 0 C = -1 D = 0 E = 0 F = 0	Panel 11	A = -6 B = -1 C = -6 D = -6 E = -5.5 F = -4
Panel 6	A = 0 B = 0 C = 0 D = 0 E = 0 F = 0	Panel 12	A = -6 B = already loose C = -6 D = -6 E = -6 F = -6

Table 3.2: Iterations made to remove panel overlaps. The already loose bolts were tightened and the panel realigned with the next adjacent panel.

3.3 Automating the Iteration Procedure

After multiple sessions of panel iteration, the best-fit shape described in Equation (2.1) had still not been attained with sufficient accuracy. The initial approach of reading the adjustment values off the colour bar, termed 'eyeballing', is imprecise for the following reasons:

1. Fractional mm values are hard to read accurately by merely looking at the colour bar.

2. Positions of adjustment points (bolts) on the surface profile can be incorrectly located and hence inaccurate reading of their mm values from the colour bar.

To overcome these uncertainties and also to streamline the adjustment process, we improved the codes to automate the adjustment numbers. This code is now referred to as the automation of adjustment (AoA) code.

The AoA Code

The AoA code infers the mm adjustment values on a bolt from interpolation by using the x and y coordinates of the errors and the bolts (shown in Figure (3.2)). These mm adjustment values are then converted to number of turns (described in panel iteration (1)).

'Eyeballing' Approach vs AoA Code.

We compared the iteration values determined by the 'eyeballing' approach and the AoA code by testing both approaches against the 85° elevation result of 21 June 2014 measurement. The panels were iterated for this measurement by 'eyeballing' because the AoA code had not been written at the time. The mm adjustment values for Figure (3.10)a using the two approaches, are shown in Table (3.3). The table is a post analysis of the iterations made by 'eyeballing' to determine the precision of the AoA code. The mm adjustment values in bold are AoA mm values which deviates from the 'eyeballing' values by wrong directional adjustment (lifting or lowering) of a panel and also half or more than 0.5 mm. The human error associated with the 'eyeballing' approach is evident in the plot of the 'eyeballing' approach versus the AoA code for the iteration values in Figure (3.10)b. We expect the surface quality to be reached quicker with this AoA code approach in future iterations.

Panel Number	Eyeballing	AoA Code	Panel Number	Eyeballing	AoA Code
Panel 1	A = -3.0	**A = -1.2**	Panel 7	A = -2.0	**A = -1.3**
	B = 2.0	**B = 0.4**		B = -2.0	B = -1.8
	C = 1.0	**C = 1.6**		C = 0.0	C = 0.3
	D = 2.0	D = 1.7		D = 0.0	D = 0.1
	E = 1.0	E = 1.0		E = 1.0	E = 1.6
	F = 1.0	F = 0.9		F = 1.0	**F = 1.8**
Panel 2	A = 3.0	A = 2.6	Panel 8	A = -1.0	A = -0.9
	B = -1.0	**B = -0.2**		B = 0.0	**B = 0.5**
	C = 2.5	**C = 1.5**		C = 1.0	C = 1.2
	D = 0.5	D = 0.0		D = 1.0	**D = -0.1**
	E = 0.5	E = 0.8		E = 2.0	E = 1.9
	F = 0.5	F = 0.7		F = 1.0	**F = 2.0**
Panel 3	A = -3.0	A = -2.7	Panel 9	A = -1.0	A = -1.2
	B = -2.0	B = -2.2		B = 0.0	B = 0.1
	C = -1.0	C= -1.1		C = 0.0	C = 0.3
	D = -1.0	D = -0.8		D = 0.5	**D = -0.2**
	E = -0.5	**E = 0.7**		E = 0.0	**E = 2.1**
	F = -0.5	**F = 0.7**		F = 0.0	**F =2.0**
Panel 4	A = -1.0	**A = -0.5**	Panel 10	A = -0.5	A = -0.8
	B = -1.0	**B = 0.1**		B = 0.0	B = -0.2
	C = 0.0	C = -0.2		C = 0.0	**C = 0.9**
	D = 0.5	D = 0.5		D = 0.0	**D = 1.2**
	E = 0.5	E = 0.7		E = 0.0	**E = 1.9**
	F = 0.5	F = 0.8		F = 1.0	**F = 1.8**
Panel 5	A = -1.0	**A = 0.6**	Panel 11	A = 0.0	A = -0.4
	B = -1.0	B = -0.7		B = -1.0	B = -1.2
	C = 2.0	C = 1.6		C = -1.0	**C = -0.2**
	D = 1.5	**D = 2.1**		D = -1.0	D = -0.9
	E = 1.0	E = 0.9		E = 1.0	**E = 1.6**
	F = 1.0	F = 1.0		F = 0.5	**F = 1.4**
Panel 6	A = -3.0	**A = -1.7**	Panel 12	A = -1.0	**A = -2.0**
	B = -3.0	B = -3.2		B = 0.0	B = -0.4
	C = 0.0	**C = 1.3**		C = -0.5	C = -0.5
	D = 0.0	**D = 0.5**		D = 1.0	D = 0.9
	E = 0.5	**E = 1.1**		E = 0.5	**E = 1.2**
	F = 0.5	**F = 1.3**		F = 1.0	F = 1.1

Table 3.3: Adjustment values (in units of mm) used for panel iteration of 21 June 2014 measurement by 'eyeballing' approach, and those predicted by the AoA code. The mm values in bold text indicate the errors (identified by the AoA code) associated by 'eyeballing'. These errors led to panel misalignments and a reason why the expected 0.5 mm RMS was not achieved.

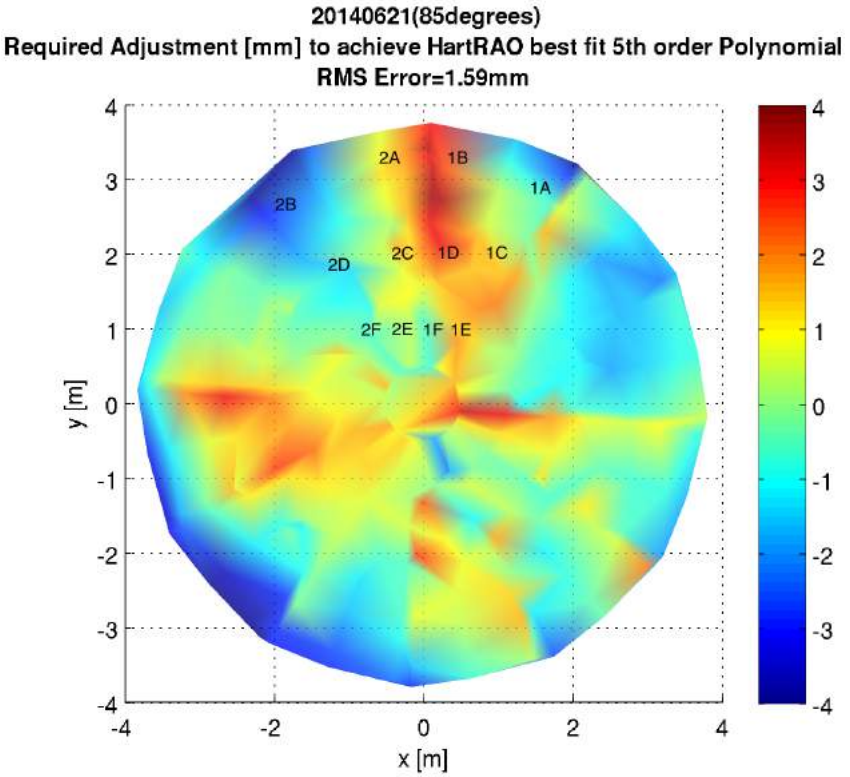

(a) 21 June 2014 measurement at el = 85° showing bolt positions on Panels 1 and 2.

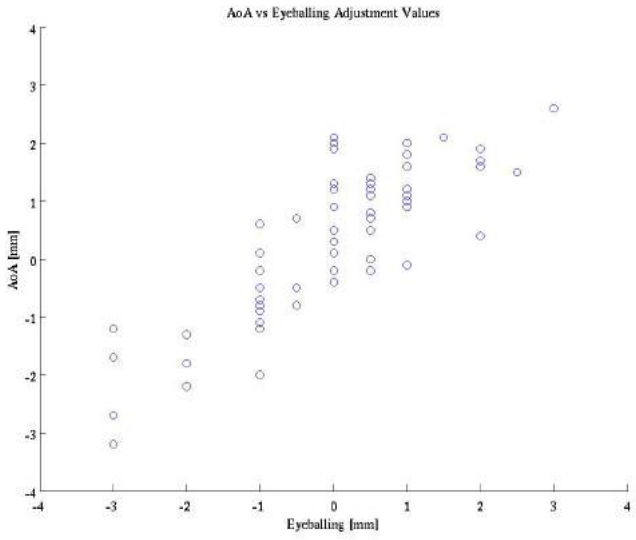

(b) A graph of the adjustment values predicted by the AoA code and the adjustments made by 'eyeballing' for the 21 June 2014 measurement in Figure (3.10)a. The adjustment values are skewed more towards the prediction by the AoA code hence indicates the human error associated with adjusting panels of the primary reflector by 'eyeballing' adjustment values from the colour bar.

Figure 3.10: Comparing the adjustment values made by 'eyeballing' and those predicted by the AoA code for 21 June 2014 measurement.

3.4 Primary Surface Analysis using Different Photographs

We regenerated the colour plots for 4 June 2015 measurement (at el = 85°) using different set of photographs of the primary reflector taken on the same day and the results are shown in Figure (3.11a, 3.11b, and 3.11c). The colour plots show panel misalignments and the need for iteration to obtain the desired shape of the primary reflector described in Equation (2.1).

We took over fifty photographs of the primary reflector during the measurement. These photographs were then divided into three independent sets, and we analysed each set separately with PhotoModeler; the resulting surface models are referred to as Model0, Model, and Model2. The purpose of this analysis was to assess the repeatability of the modelling process and the robustness of the PhotoModeler software.

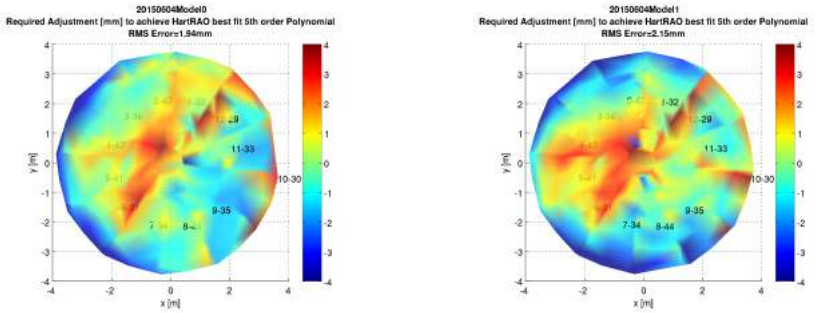

(a)

(b)

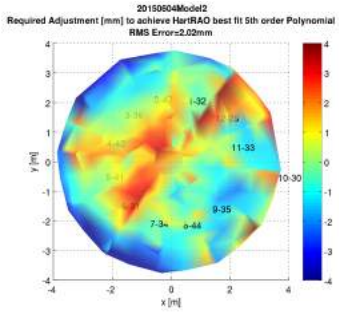

(c)

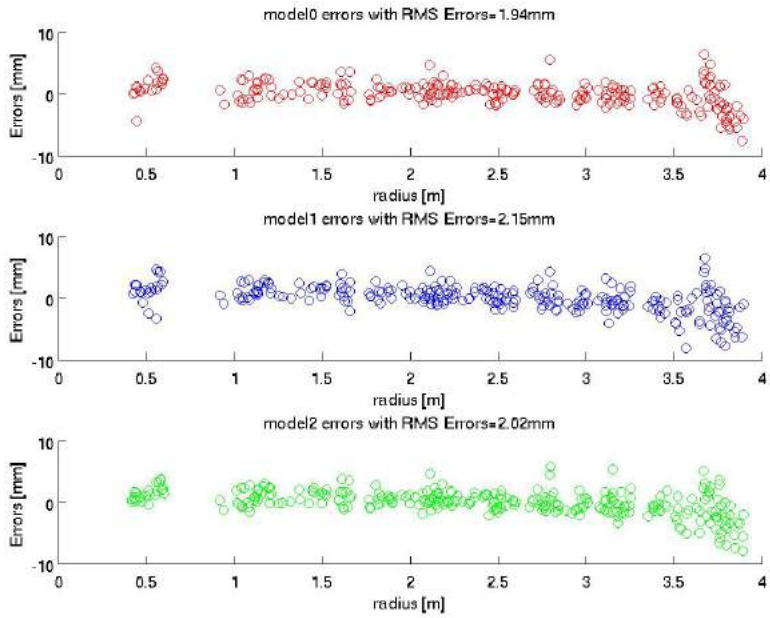

(d) The deviations in Figure (3.11a, 3.11b and 3.11c) plotted over the radius of the primary reflector with their respective RMS errors. The deviations plotted here are those determined by the AoA code. These deviations are the required adjustment values on the various panels to achieve the desired shape described in Equation (2.1).

Figure 3.11: Plots (a), (b), and (c) are the deviations of panel positions from the desired shape in Equation (2.1) as determined from Model0, Model1, and Model2 photographs respectively. Plot (d) compares the adjustment values predicted by the AoA code for all three models. The comparison allows us determine the accuracy of our photogrammetry measurements and panel iterations.

The RMS errors varied with maximum of ∼0.2 mm which is comparable to the result in Figure (3.4). The 0.2 mm error in the results from the three models still do not indicate whether, the error is from our measurements or real systematics. The deviations due to each model are shown in Figure (3.11)d. There are slight variations (within 0.5 m and 3.5 to 4m radii) in required adjustment values proposed by each of the models as shown in Figure (3.11)d. In future measurements, we will take multiple photogrammetry measurements at a single elevation on the same day and compare the results so we can quantify whether the error is due to our measurements or systematics. Possible systematics that could cause panel misalignments are fractional number of bolt turns that are difficult to achieve (eg. 0.6 bolt turns) and inaccurate directional turn of bolts leading to inaccurate lowering or lifting of panels. In future measurements, we shall generate colour profiles using different photographs and quantifying the source of the errors due to different models will help identify which model is best for iterating panels.

3.5 November 2015

After the overlapping panels were separated, photogrammetry measurement was carried out at el = 45° and the result is shown in Figure (3.12)a. As a test of the accuracy of the code, panels in November results were iterated using 2 to 3 mm short of the real values determined by the code. We iterated 1A, 7B, 8A, (9A, 9D), (10B, 10C) and 12B by +10, +5, +5, (+2, -5), (+2, -5) and +10 mm respectively of Figure (3.12)a. After the iteration, we took photographs of the primary reflector at el = 5° during the day and the result is shown in Figure (3.12)b.

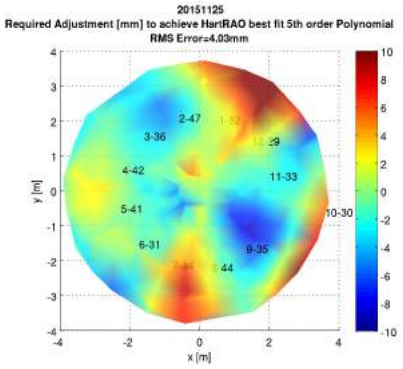

(a) State of the dish after panel overlaps were removed. Measurement was taken at el = 45°.

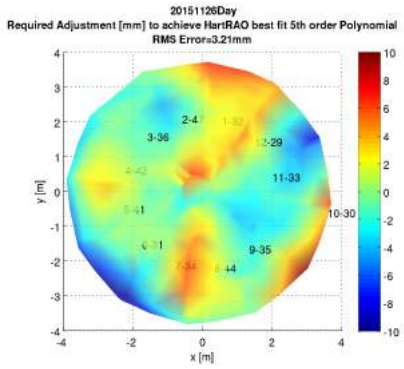

(b) We proved day-time photogrammetry is possible and the RMS decreased from 4.03 mm to 3.21 mm. We took the measurement at el = 5° due to safety against strong winds on site.

Figure 3.12: All iteration values used in November were determined from the AoA code.

We then iterated the panels in Figure (3.12)b with the iteration values shown in Table (3.4). After the iteration, we carried out the final photogrammetry measurement in 2015 and the result is shown in Figure (3.13). This figure shows the current state of the primary reflector at the time of submission of this dissertation.

Panel Number	mm Value	Panel Number	mm Value
Panel 1	A = +3 B = +4 C = +2 D = +2 E = 0 F = 0	Panel 8	A = 0 B = 0 C = Align with 7D D = 0 E = 0 F = 0
Panel 2	A = +4 B = 0 C = Align with 1D D = 0 E = 0 F = 0	Panel 9	A = 0 B = +4 C = 0 D = Align with 10C E = 0 F = 0
Panel 5	A = 0 B = Align with 6A C = 0 D = 0 E = 0 F = 0	Panel 10	A = Align with 9B B = 0 C = -2 D = -2 E = 0 F = 0
Panel 6	A = -3 B = -4 C = 0 D = 0 E = 0 F = 0	Panel 11	A = 0 B = -4 C = 0 D = 0 E = 0 F = 0
Panel 7	A = Align with 6B B = 0 C = 0 D = +4 E = 0 F = 0	Panel 12	A = Align with 11B B = Align with 1A C = 0 D = Align with 1C E = 0 F = 0

Table 3.4: 26 November day iteration values made on panels in Figure (3.12)b.

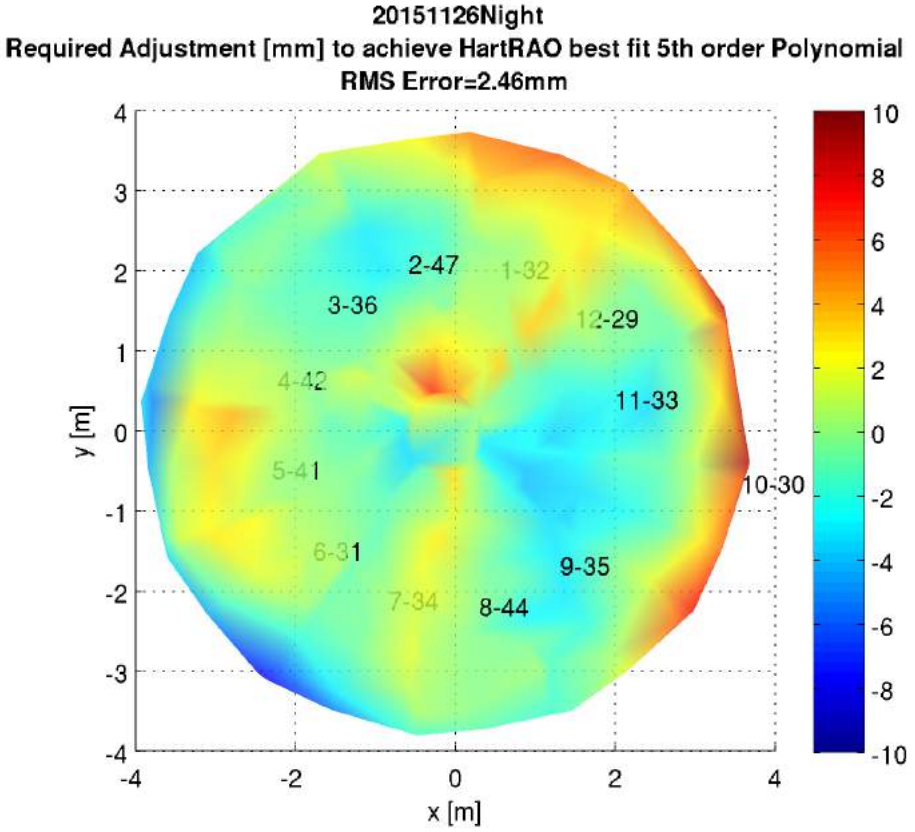

Figure 3.13: The current state of the primary reflector at the time of submission of this dissertation. The average panel misalignment (or RMS error) is 2.46 mm. In the future, more panel iterations shall be made to achieve the desired 0.5 mm RMS error.

3.6 Summary of all Photogrammetry Measurements

A summary of all photogrammetry measurements taken up to the time of submission of this dissertation is shown in Table (3.5).

Date	el	RMS Error (mm)	Iteration?	Note
13 May 2014	5°	6.03	Yes	Panel 1 lifted as reference
16 May 2014	5°	3.68	Yes	Improved
25 May 2014	5°	3.48	Yes	Improved
26 May, 2014	—	—	—	Panel 1 lowered
21 Jun 2014	5°, 45°, 85°	1.78, 1.57, 1.59 resp.	No	Small variation at different el
23 Jun 2014	85°	1.17	Yes	Improved
27 Jun 2014	85°	1.15	No	Improved
30 Sept 2014	85°	1.15	Yes	Panels are stable
4 Oct 2014	85°	1.19	Yes	Wrong adjustment points
5 Oct 2014	85°	1.75	Yes	Wrong adjustment points
7 Oct 2014	85°	4.89	Yes	Panel 1 lifted again
9 Oct 2014	85°	2.01	Yes	Panel 1 lowered
20 Jan 2015	85°	2.14	Yes	Few panels iterated
4 Jun 2015	85°	1.94	—	Separating overlapping panels
25 Nov 2015	45°	4.03	Yes	Overlapping panels separated
26 Nov 2015 Day	5°	3.21	Yes	Improved
26 Nov 2015 Night	5°	2.46	Not yet	Iteration will be done

Table 3.5: Results of all photogrammetry measurements.

The primary reflector is currently in a state described in Figure (3.12)c with average panel deviations of 2.46 mm. The expected 0.5 mm average panel deviations was unattainable because only a few panels were iterated after the overlapping panels had been separated. The iteration of only few panels was primarily to test the accuracy of the AoA code. The AoA code was good and accounted for the sharp fall in the average panel deviations for 25 Nov - 26 Nov 2015 Night measurements shown in Table (3.5) even though only a few panels were considered.

In the future, all surface profile analysis of the primary reflector shall be done using the AoA code, and all twelve panels of the primary reflector shall be iterated to achieve the 0.5 mm RMS quickly.

3.7 General Reflector Antenna Software Package simulations of the Primary Reflector

This section shows General Reflector Antenna Software Package (GRASP) simulations of the ideal beam according to our specification in Subsection(2.7) and the predicted sidelobes due to surface errors. GRASP determines the beam patterns by adding to an existing reflector, the surface error data taken from photogrammetry measurements. The CBASS telescope is modelled in GRASP by using a computer simulation technology model of the CBASS design for the feed and one-dimensional surfaces with assumed rotational symmetry for the primary and secondary reflectors. The order in which the telescope beam was simulated includes the re-illumination of the sub-reflector by the primary (ray path - feed - sub-reflector - primary - sub-reflector - sky), as well as the subsequent secondary re-illumination of the primary (feed - sub-reflector - primary - sub-reflector - primary - sky). The modelling in

GRASP considered the blockage caused by the sub-reflector which affects the main beam and inner sidelobe shape and forward gain. The GRASP model also accounted for the blockage of the sub-reflector by the primary which gives a low backlobe.

Figure (3.14)a shows the predicted beam using the 4 June 2015 photogrammetry results. The loss in forward gain is about 1.2 dB (η_s of 0.76). The first sidelobe is very asymmetric, with a amplitude of -15 dB relative to the peak, compared with -21 dB for the ideal case. This level of sidelobe asymmetry is too high and would increase the noise level in our receiver when measuring the power of point sources and galaxies.

In Figure (3.14)b, the deviation from ideal performance scales roughly logarithmically with the surface distortions; the forward gain loss is 0.6 dB (η_s of 0.87) for half-scale errors and 0.3 dB (η_s of 0.92) for quarter-scale errors. With our goal of forward gain loss less than 10%, we need to aim for surface distortions around one quarter of their current values (0.25 x 1.94 mm = 0.5 mm).

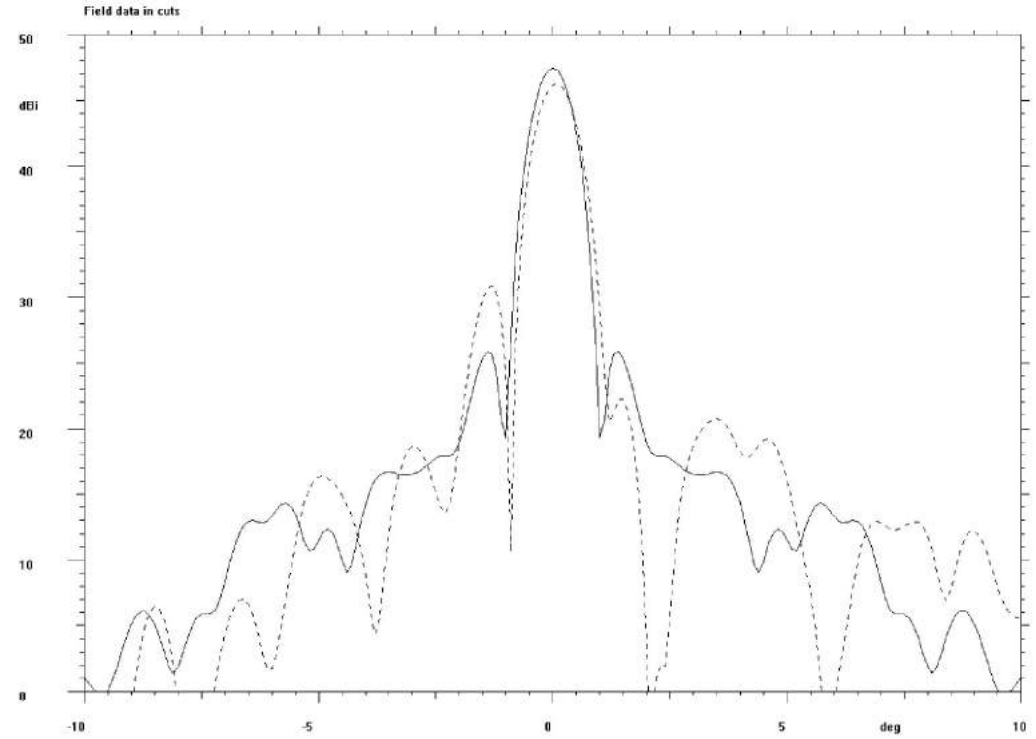

(a) Solid line: Ideal beam pattern. Dashed line: Beam calculated from the 4 June 2015 photogrammetry data.

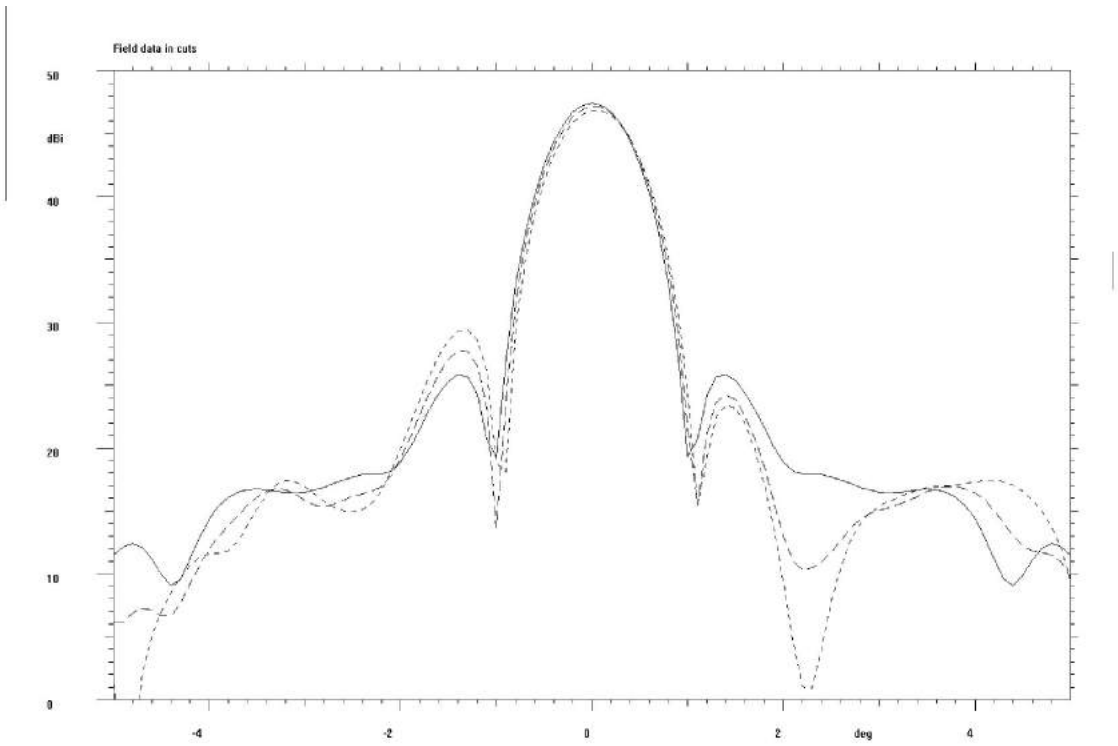

(b) Solid line: CBASS ideal beam pattern. Short line: Surface distortions scaled to a half of 4 June 2015 values. Long dashed line: Surface distortions scaled to a quarter of 4 June 2015 photogrammetry data.

Figure 3.14: GRASP simulations of expected CBASS beam and the obtained beam for 4 June 2015 measurement. Images: Mike Jones.

3.8 Future Outlook of CBASS Southern System

CBASS-S is currently scanning the southern sky for RFI and making synchrotron maps of the BICEP2 region. We expect the instrument to start full science operations in February 2016 after all panels of the primary reflector have been iterated and the desired forward gain achieved in January 2016.

The Daily Quality Plots

The quality plots are raw twenty-four hour data plots deposited on a user friendly webpage which provide a first look at how the telescope is performing during observations. A sample plot is shown in Figure (3.15). CBASS scans the sky in azimuth (az) at 4° per second at a fixed elevation.

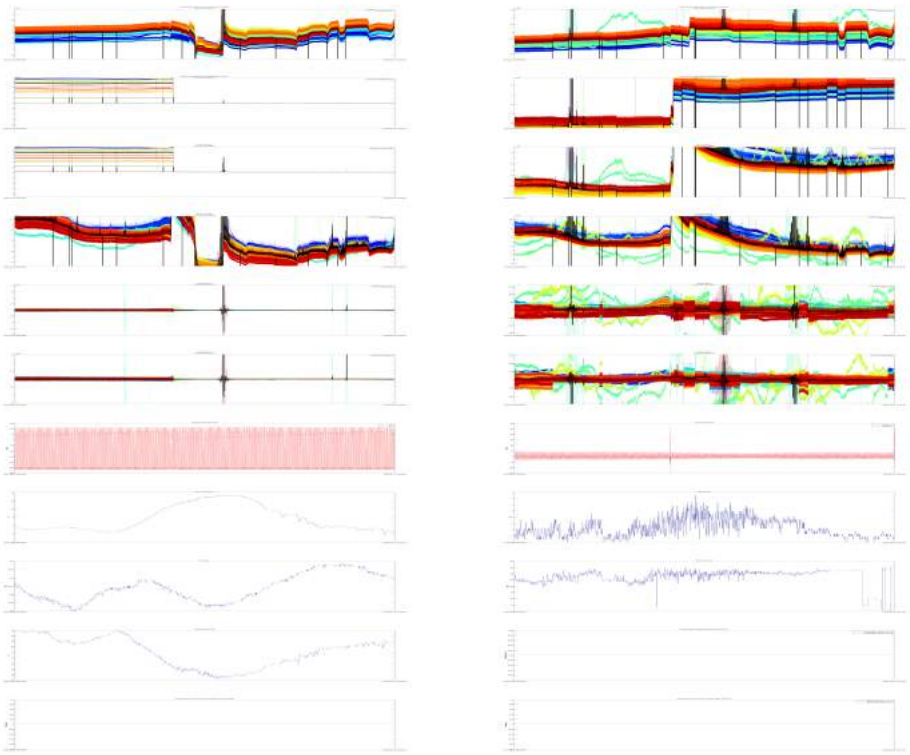

Figure 3.15: Sample quality plot for 16 June 2014. The plot will serve as a useful diagnostic tool for checking the performance of the telescope.

The rainbow colours in the ROACH plots are in Panels 1 - 12 of Figure (3.15) the frequency channels of the two CBASS ROACH boards. These plots help understand the behaviour of the various frequency channels during science observations. Frequency channels that do not appear on the plots are labelled as off-scaled channels above each plot. The off-scaled frequency channels provide information on the

total bandwidth used during an observation hence a need to critically observe those channels and determine the problems associated with them. In general, the ROACH plots help identify strange behaviour in the CBASS frequency channels. The spikes in the ROACH time streams are from the noise diode that is turned on every hour to ensure the telescope is really observing the sky.

The weather plots in Panels 15 - 19 of Figure (3.15) provide information on the weather conditions at the telescope site. These plots include air temperature and pressure, wind speed and direction and relative humidity. The air temperature and pressure and relative humidity plots generally indicate the opacity of the atmosphere. The atmospheric opacity is relevant to understanding the intensity of signals received by the telescope. Water vapour and rain drops increase the thickness of the ionosphere and reduces the intensity of incoming signals from the sky. CBASS sky-dip scans are observations used in studying the opacity of the atmosphere and the data from these scans can be cross-checked with the weather data on these plots for compatibility. The wind speed plot is useful for understanding deviations in the az and el positions during CBASS scans. Strong winds affect the pointing of the telescope and the purpose for which the wind speed plot is placed underneath the errors in az/el scan plot in Panel 14 for quick inspection.

Az/el versus time plot in Panel 13 of Figure (3.15) shows the scanning strategy such as raster scans of the telescope during an observation.

Timing difference plots in Panels 20 - 22 of Figure (3.15) are used for checking if both roaches and the roaches and servo are in synchronisation. The CBASS-S relies on the 1PPS signal from the GPS unit for all timings within the system hence a need for the roaches and servo to be synchronised. Any identified timing differences in the plots requires urgent attention at the ROACH boards and/or GPS unit.

Chapter 4

Conclusions

The primary reflector of CBASS-S has been characterised via close range photogrammetry; a 2.46 mm RMS surface accuracy was achieved. A 0.5 mm RMS surface accuracy was aimed for, however, due to panel overlaps and human error ridden approach of 'eyeballing' adjustment values, the aim was not achieved. Currently, panel overlaps have been removed and a more efficient panel surface analysis code referred to as AoA code, has been written and tested and hence we anticipate two more AoA panel iterations to achieve the final surface accuracy specification. The better than 0.9 forward gain specification for CBASS-S was deduced from the Ruze formula but GRASP simulations are used to measure the forward gain by adding to an existing reflector, the surface error data of the primary reflector from photogrammetry measurements. The simulations are also used to study the beam pattern of CBASS-S.

Through this MSc project, a standard operation manual has been written for future optimisation of photogrammetry measurements and analysis. The author of this dissertation has shown weather conditions such as wind, rain and heat on site do not affect panel alignments of the primary reflector of CBASS-S.

With CBASS-S expected to start science operations in February 2016, a user friendly webpage of data quality plots have been created. These twenty-hour time stream plots of various parameters in the system will help for quick performance monitoring of the telescope. These plots will be useful in cross checking irregularities in final CBASS maps. Such irregularities include low signal intensities, gaps in maps possibly due to inadequate data in the CBASS-S system. Inadequate data in the system may be due to faulty frequency channels or telescope shutdown.

Bibliography

[1] D. J. Fixsen, 2009. *The Temperature of the Cosmic Microwave Background.*. ApJ, 707, 916 - 920.

[2] W. Hu & M. White, 1997. *A CMB Polarization Primer*. New Astronomy 2:323-344.

[3] L. Krauss et al, 2010. *Primordial Gravitational Waves and Cosmology*. Science, 328, 989.

[4] D. Hanson et al, 2013. *Detection of B-mode Polarisation in the Cosmic Microwave Background with Data from the South Pole Telescope*. Physical Review Letters, 111, 141301.

[5] U. Seljak & M. Zaldarriaga, 1997. *Signature of Gravity Waves in Polarization of the Microwave Background*. Physical Review Letters, 78, 2054-2057.

[6] M. Kamionkowski, A. Kosowsky & A. Stebbins, 1996. *Statistics of Cosmic Microwave Background Polarization*. Physical Review D, 55, 7368-7388.

[7] P. A. R. Ade et al, 2014. Planck 2013 Results. XXII. Constraints on Inflation. A & A, 571, 42.

[8] P. A. R. Ade et al, 2014. Detection of B-Mode Polarization at Degree Angular Scales by BICEP2. Physical Review Letters, 112, 241101.

[9] P. A. R. Ade et al, 2015. *A Joint Analysis of BICEP2/Keck Array and Planck Data*. Physical Review Letters, 114, 101301.

[10] S. K. Choi & L. A Page, 2015. *Polarized Galactic Synchrotron and Dust Emission and their Correlation*. JCAP, 12, 20.

[11] C. L. Bennett et al, 2013. *Nine-Year Wilkinson Microwave Anisotropy Probe (WMAP) Observations: Final Maps and Results.* ApJS, 208, 20.

[12] H. Bradt. *Astrophysics Processes.* Cambridge University Press, New York, 2008.

[13] G. B. Rybicki & A. P. Lightman. *Radiative Processes in Astrophysics.* Wiley-VCH Verlag GmbH & Co. KGaA, Weinheim, 2004.

[14] A. Aberget et al. *Planck 2013 Results. XI. All-Sky Model of Thermal Dust Emission.* AaP, 571, A11.

[15] B. T. Draine & A. A. Fraisse, 2008. *Polarized Far-Infrared and Submillimeter Emission from Interstellar Dust.* ApJ, 696, 1-11.

[16] E. M. Leitch. *A Measurement of Anisotropy in the Microwave Background on 7′-22′ Scales.* PhD thesis, California Institute of Technology, 1998.

[17] B. T. Draine & A. Lazarian, 1997. *Diffuse Galactic Emission from Spinning Dust Grains.* ApJL, 494, L19 - L22.

[18] P. Reich, J. C. Testori & W. Reich, 2001. *A radio continuum survey of the northern sky at 1420 MHz.* A & A, 376, 861-877.

[19] M. W. Peel et al, 2012. *Template fitting of WMAP 7-year data: anomalous dust or flattening synchrotron emission*?. MNRAS, 424, 2676-2685.

[20] C. M. Holler at al, 2012. *A Circularly Symmetric Antenna Design With High Polarization Purity and Low Spillover.* IEEE Transactions on Antennas and Propagation, 61, 117-124.

[21] J. Ruze, 1966. *Antenna Tolerance Theory—A Review.* Proceedings of the IEEE, 54, 633-640.

[22] C. J. Copley. *C-Band All-Sky Survey.* PhD thesis, University of Oxford, 2013.